



UNIVERSITAT POLITÈCNICA DE CATALUNYA
BARCELONATECH

**Escola Tècnica Superior d'Enginyeria
de Telecomunicació de Barcelona**

**Validation of the new depolarization channel at 532 nm of the
UPC multi-wavelength lidar**

A Master's Thesis

Submitted to the Faculty of the

**Escuela Técnica Superior de Ingeniería de Telecomunicación de
Barcelona**

Universitat Politècnica de Catalunya

by

Enis Ben Chahed

In partial fulfilment

of the requirements for the degree of

MASTER IN TELECOMMUNICATIONS ENGINEERING

Advisor: Michaël Sicard

Barcelona, September 2017



Title of the thesis: Validation of the new depolarization channel at 532 nm of the UPC multi-wavelength lidar

Author: Enis Ben Chahed

Advisor: Michaël Sicard

Abstract

The Remote Sensing Laboratory (RSLab) in Universitat Politècnica de Catalunya (UPC) operates a 7-channel lidar to detect atmospheric particles. The multi-wavelength characteristic of the system allows for the use of advanced techniques and methods to retrieve, not only the aerosol optical properties, but also information on their size, shape, etc...

The purpose of this project is to assess the proper functioning of the new depolarization channel at 532 nm. This channel, installed in 2016, measures the quantity of light backscattered with a polarization direction perpendicular to the emitted one. We first use the optical software Zemax to make the raytracing of the actual optical setup in order to verify the correct arrangement of all the components within the optical channel. Then, a detailed analysis of the two received powers of interest (total and perpendicular) is described. The procedure and the stability of the calibration over the last 18 months is presented.

Finally, the retrieval of the volume and particle depolarization ratios and their associated error bars is described. The validation of these products (volume and particle depolarization ratios) is made by comparison with the same quantity retrieved from a co-located lidar.

At the very end, retrievals under different atmospheric scenes (low and high mineral dust loads, clouds) are presented as illustration.



*To my family.
For all their efforts and their never-ending support.*

ACKNOWLEDGMENTS

My deepest thanks go to my advisor, professor Michaël Sicard, for accepting me at UPC and for having wisely guided me throughout this special journey during the past six months.

I am also indebted to him for allowing me to present my work during RICTA, a scientific conference where I had the chance to figure out a little more how the researchers' world looks like.

Furthermore, I would like to express my gratitude to all the professors whom I have worked with, especially Alejandro Rodríguez and Adolfo Comerón, for assisting me many times with the same endless patience and generous willingness that characterize them.

And finally, a huge thank you to Ruben, Maria José and Nikos for the pleasant and funny moments I spent with them and for the kind and long-lasting support they gave me.



Revision history and approval record

Revision	Date	Purpose
0	25/08/2017	Document creation
1	29/08/2017	Document revision

Written by:		Reviewed and approved by:	
Date	25/08/2017	Date	01/09/2017
Name	Enis Ben Chahed	Name	Michaël Sicard
Position	Project Author	Position	Project Supervisor

Table of contents

Abstract	3
Acknowledgements.....	5
Revision history and approval record	6
Table of contents	7
List of Figures	9
List of Tables.....	12
Chapter 1: Introduction	14
1.1. Monitoring of the atmosphere	14
1.1.1 Why is it so important?.....	14
1.1.2 Aerosols characterization.....	15
1.2. LIDAR	15
1.2.1 Remote monitoring of the atmosphere.....	15
1.2.2 Principles of LIDAR technique and optical phenomena.....	16
1.3. Objective of this thesis	18
Chapter 2: The UPC Lidar system and the new depolarization channel at 532 nm	19
2.1. The Lidar system.....	19
2.1.1 Lidar equation.....	19
2.1.2 UPC Lidar system description.....	22
2.2. The new depolarization channel at 532 nm.....	25
2.2.1 Introduction.....	25
2.2.2 Schematic and description of the optical components.....	26
2.2.3 δV and δP retrieval with this configuration.....	28
Chapter 3: Optical characterization of the new depolarization channel at 532 nm	32
3.1. The TAIR-3S Telephoto lens	32
3.1.1 Introduction.....	32
3.1.2 Zemax procedure and results.....	33

3.2. Optical characterization	37
3.2.1 Complete analysis of the channel.....	37
3.2.2 FOV evaluation and final spot.....	40
Chapter 4: Calibration of the new depolarization channel at 532 nm	44
4.1. Calibration method	44
4.1.1 The System Channel Ratio retrieval.....	44
4.1.2 Daytime and night-time calibrations.....	46
4.2. Matlab Implementation	48
4.3. Calibration stability	49
4.3.1 Calibration profiles over time and error budget.....	49
4.3.2 Calibration over temperature.....	51
Chapter 5: Retrieval of volume and particle depolarization ratios	52
5.1. Comparison with SCC	52
5.2. Comparison with MPL	57
5.3. Analysis of different aerosol load situations.....	59
Chapter 6: Conclusions and future development.....	67
Appendices	70
Bibliography	79

List of Figures

1.1	Schematic of the operating principle of a LIDAR. The emitted light gets through an aerosol layer causing reflections, absorptions and other optical phenomena.....	16
1.2	Example of three different particle shapes. According to the shape there will be a stronger or weaker depolarization.....	17
2.1	Example of aerosol characterization taken from U. Wandinger et al ^[12] . The combination of Lidar ratio, Colour ratio and particle depolarization ratio is what allows a reliable typing of aerosols species.....	22
2.2	a) Picture of the complete system. In the middle is the main telescope. On the right the auxiliary one, while on the left is the Q-switched laser. b) Sketch of the Polychromator: input light coming from the fibre bundle (on the top left) encounters a set of dichroic filters, lenses and mirrors which split it in 6 different channels c) the same polychromator represented on AutoCAD.....	23
2.3	Schematic of the emission and reception set up.....	25
2.4	Overall layout of the optical channel.....	26
2.5	Schematic of FOV computation.....	27
3.1	Sketch of theTAIR-3S set of lenses.....	32
3.2	Sketch of the complete optical channel.....	37
3.3	Complete scheme of assembly parameters of the optical channel.....	39
3.4	2D Zemax representation of the whole channel.....	40
3.5	3D Zemaz representation of the whole channel.....	40
3.6	Pictures of the PMT surface reached by the two outermost light beams (corresponding to a total FOV of 3.14 mrad).....	42
3.7	Picture of the PMT surface reached by a perpendicular light beam.....	43



3.8	Picture of the PMT surface reached by all the light beams: perpendicular and oblique ones. Blue for the perpendicular rays, red and green for -1.57 mrad and +1.57 mrad respectively.....	43
4.1	a) Difference between Photon-Counting (PC) and analog detection mode. b) Gluing between PC and Analog signals. It can be seen how the gluing coincides with PC at high altitude (where analog signal is noisy), while at low altitudes it coincides with the analog one.....	47
4.2	Result of the average (yellow) performed between $\delta^*(90^\circ + 45^\circ)$ and $\delta^*(90^\circ - 45^\circ)$ and its smoothing (pink). The filtered pink curve is the so-called calibration vector.....	48
4.3	Overview of all the calibrations vectors over time.....	49
4.4	Display of all calibration vector far range values over time. Realignment dates are also highlighted.....	50
4.5	Matrix representation of the piecewise normalized distance.....	51
4.6	Sketch of the relationship between calibration far range value and environment temperature. On the right, the colour scale distinguishes the most recent calibration from the oldest.....	52
5.1	Comparison between dV and dP derived with UPC and SCC algorithms from a 60 min daytime measurement on 20/06/2016 at 18:44 UT.....	54
5.2	Comparison between dV and dP derived with UPC and SCC algorithms from a 150 min night-time measurement on 06/07/2016 at 00:47 UT.....	54
5.3	Comparison between dV and dP derived with UPC and SCC algorithms from a 60 min daytime measurement on 19/03/2017 at 15:44 UT.....	55
5.4	Comparison between dV and dP derived with UPC and SCC algorithms from a 150 min daytime measurement on 28/03/2017 at 00:45 UT.....	55
5.5	Comparison between dV and dP derived with UPC and SCC algorithms from a 150 min daytime measurement on 13/04/2017 at 00:45 UT.....	56
5.6	Comparison between dV and dP derived with UPC and MPL	57
5.7	Comparison between dV and dP derived with UPC and MPL	57
5.8	Comparison between dV and dP derived with UPC and MPL	58

5.9	Picture 5.9 shows three successive measurements performed in two days (16-17/05/17) within LRMC campaign. It is possible to notice how during the central measurement the accordance between the two systems fails while it is recovered in the early morning measurement of the following day.....	5
5.10	Volume depolarization ratio of an aerosol layer at low altitude.....	61
5.11	Comparison of volume and particle depolarization ratio.....	62
5.12	Daytime comparison between Volume and Particle depolarization ratio.....	62
5.13	Volume depolarization ratio in presence of a low cloud. The screening induced does not allow power to get through.....	63
5.14	MODIS map of the cloud event on 03/03/2017.....	63
5.15	Saharan dust intrusion: such a phenomenon induced a peak in the volume depolarization ratio.....	64
5.16	Pictures 5.6 and 5.7 depict the volume and particle depolarization ratio profiles at two different hours, highlighting the presence of two layers of Saharan dust the first of which is holding steady at 1.5 km over time while the second progressively drops down. MPL volume depolarization ratio is also pictured showing great accordance between the two different systems. Picture 5.16 gives a distinct perspective showing how dV varies over the whole measurement hours.....	65
5.17	Picture showing a weaker phenomenon of Saharan dust intrusion on 07/06/2016. In this case volume depolarization ratio is below 10%.....	66

List of Tables

2.1	List of the optical component and their features.....	27
3.1	Physical parameters of the Telephoto lenses.....	34
3.2	Optical parameters of the Telephoto lens according to the trial-and-error approach and Zemax approximation. Such values are assessed by means of thick lens analysis. (see appendix B)	35
3.3	2D-3D layouts and focused spot of TAIR-3S according to the two approaches with axial rays.....	36
3.4	Features of the objects employed in the channel.....	38
3.5	List of distances between channel components.....	39
3.6	List of the percentage of rays impinging on the PMT surface at different angles.....	40
3.7	Summary of the results of the channel optical characterization.....	44



Chapter 1

Introduction

1.1: Monitoring of the atmosphere

1.1.1: Why is it so important?

The analysis of the components of the atmosphere has been always considered of primary importance due to the impact they have on climate change and, consequently, on human life. Besides studying the intrinsic composition of the atmosphere (mostly gases), in recent years the discovery of the presence of floating particulate matter drew scientists' attention to the consequences they can have on Earth environment. Such particles, denominated aerosols, have the capability to influence life on Earth at many distinct levels due to their vast variety of dimensions (which, on average, range from few nanometers to few tens of micrometers). The analysis of such impacts is considered to be of utmost importance.

A significant push towards the development of studies in this field came after realizing that man's activities since the industrial revolution play a major role in the formation of pollutants particles which cause dramatic effects on the environment.

The worsening of air quality due to the presence of some of these aerosols causes both direct and indirect damages on human life: on one side, affecting directly the air that we breath, polluted aerosols are proved to cause most of the widespread respiratory and cardiovascular diseases (short-term consequences); and, on the other side, the presence of aerosols influences Earth radiative budget^[1] because of the alteration of solar radiation impinging on our planet and, as a consequence, the induced effects on climate change have always been considered by the IPCC (Intergovernmental Panel on Climate Change, the international body which establishes and assesses climate-related policies) as a source of concern about the future climate predictions.

The accomplishment of a detailed analysis in this field must necessarily start with a deep understanding of the atmospheric constituents at stake and this is why particle characterization is the most appropriate way to fulfil this task to date.

1.1.2: Aerosol characterization

Aerosol monitoring is very challenging because of the huge diversity (on very different scales: dimensions, chemical species, effects etc..) of aerosol present in our atmosphere and the ease with which they are moved from their source region. In addition, depending on the places where they are originated and the physical and chemical processes they undergo, aerosols of the same species can manifest different behaviours.

Aerosols properties can be subdivided into several types: chemical, optical, microphysical, just to mention a few. These properties are often related to the source of the aerosols which can be either natural or anthropogenic.

For instance, natural aerosols can be released in the atmosphere by wildfire smokes (biomass aerosols that come from burning vegetation), volcanoes eruptions (sulfate particles which are formed after the emission of sulfur dioxide) or mineral dust coming from the wind erosion of vast desert areas (of which Sahara is one the most important).

Anthropogenic aerosols are, on the contrary, the most abundant aerosol type in industrialized areas in the northern hemisphere and they are originated mainly from combustions of fossil fuel (which release mainly Organic Carbon and Black Carbon, as well as Nitrates which come from the Oxidation of NO_x) such as industry and traffic emissions.

1.2: LIDAR

1.2.1: Remote monitoring of the atmosphere

Historically, the techniques exploited by scientists to analyze the composition of atmosphere samples were of chemical type. They basically consisted in sensing the atmosphere in-situ in a very precise location and then in bringing the sample in a laboratory to perform the required analysis. Though very accurate, this kind of study is limited by single-point measurements.

In the past decades, such measurements started to be improved thanks to *remote sensing techniques*, which granted both the capability to investigate chemical and physical parameters which are present in an environment spatially separated from the instruments and great accuracy of the results.

Among the many types of remote sensing techniques which have been developed, optical techniques, thanks to the great improvements of laser technology, began to be the most employed because of technological progresses made in detectors working in the optical spectrum and the vast variety of information (optical properties, size, shape, etc.) which can be acquired thanks to this kind of analysis in this spectral range.

1.2.2: Principles of LIDAR technique and optical phenomena

LIDAR (Light Detection and Ranging) is a remote sensing technique which employs the light emitted by a laser to get information about several atmospheric parameters among which aerosol properties. The principle of working is the following: thanks to a pulsed monochromatic light beam emitted by a laser, it is possible to analyze the atmosphere constituents collecting and measuring the backscattered light. Of course, the working frequency as well as the energy and the durations of the pulses are parameters that depend on the required application.

The most common laser employed in this field are Q-switched ruby or Nd:YAG laser which emit at 694 nm and 1064 nm respectively.

As laser light passes through the layers of the atmosphere, particles and molecules cause spread scattering and absorption. Some of the scattered energy is reflected backward in the direction of the incident light source ($\vartheta = 180^\circ$).

The reflected light is collected by means of a telescope then filtered and processed

A simple schematic is shown in fig 1.1.

The processing of the acquired information starts with the conversion (usually performed by a photodetector) of the incoming light into an electric signal whose intensity depends on the power intensity of received light pulse.

Of course, emitted light is not entirely reflected by aerosols. In fact, if the energy of the photons complies with the absorption band of the molecules encountered in the atmosphere, they get absorbed and the beam is said to be attenuated.

For this reason, a powerful light source is usually employed.

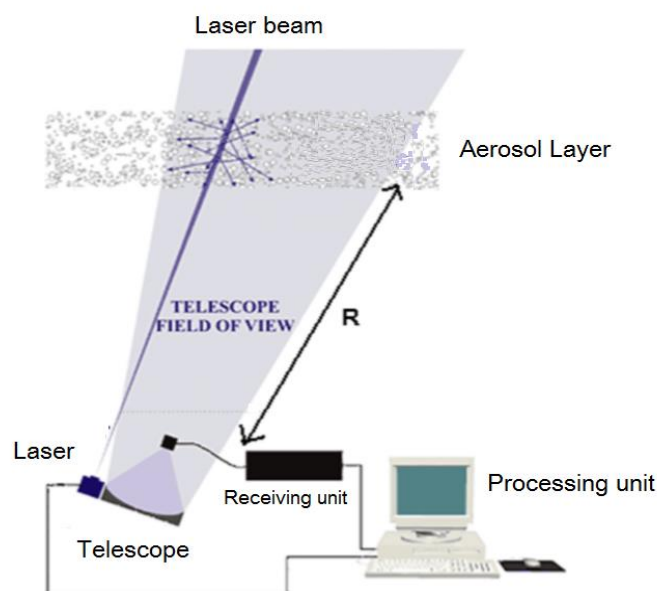


fig 1.1

Schematic of the operating principle of a Lidar.

The emitted light gets through an aerosol layer causing reflections, absorptions and other optical phenomena.

Adapted from E. V. Calvo. [2]

The necessity to have a monochromatic light beam lies in the fact that this technique is mostly based on *Rayleigh scattering*. This is the most common case of elastic scattering, namely, a type of reflection in which the frequency and, consequently, the energy of the incident photon is preserved.

Knowing the output frequency, one can isolate that frequency from the broad spectrum of the collected light by means of an interferential filter.

However, it is important to mention that elastic backscattering is not the only phenomenon involved. In fact, because of rotational and vibrational energy levels of molecules, another common phenomenon which takes place as light propagates through atmospheric layers is the so-called *Raman scattering*.

According to this phenomenon, the photons impinge inelastically on the molecules giving rise to energy levels excitation which causes a change of energy of the incident photon. This eventually causes a shift in the wavelength of reflected light.

Thanks to this important phenomenon another level of characterization is possible.

In fact, the magnitude of the frequency shift is related uniquely to a precise molecule because the difference of emitted and received frequencies is equal to the energy difference between the final and initial state of the molecule, while its intensity is proportional to the molecule's concentration.

Finally, the last important phenomenon that takes place when dealing with polarized light sources is the so-called *Depolarization*, extremely useful for aerosol typing ^{[3][4]}.

According to this phenomenon, depending on the shape of the encountered particle, the scattered light can have a different polarization than the incident one.

In fig 1.2 few examples of particle shapes are sketched.

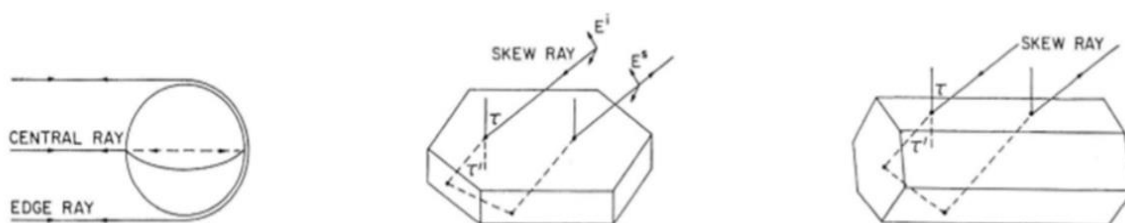


fig 1.2

Example of three different particle shapes. According to the shape there will be a stronger or weaker depolarization.

Image courtesy of K. Sassen ^[5]

This phenomenon is extremely important as, with it, a deeper level of analysis can be achieved. Intuitively, the more irregular is the shape of the particle, the higher will be the level of depolarization induced and vice versa.

For instance, a dust particle which is irregularly shaped (by the wind erosion, for example) can induce a high level of depolarization while a perfectly spherical particle causes no depolarization whatsoever ^[6].

1.3: Objective of this thesis

The topic of this project is the validation of the recently-installed depolarization channel working at 532 nm. This new channel was added to UPC lidar system in March 2016 to improve the level of characterization and typing of aerosol exploiting the depolarization phenomenon. The RSLab of the UPC is member of EARLINET (the European Aerosol Research Lidar Network), a research project which involves 28 lidar stations spread all over Europe. EARLINET works with the aim of creating a huge database of information about aerosols and their distribution across the continent.

Being made of several components, the first task is the verification of the correct arrangement of all the building blocks of this new channel, starting from the equipped telescope and then with all the other optical elements forming part of the channel. To do this, the optical software Zemax is used to work with its raytracing tools thanks to which a detailed analysis is possible. The results of these simulations and the comparison with the predicted theoretical results are shown in Chapter 3.

In Chapter 4, an accurate description of the calibration procedure between the two channels working at 532 nm is provided. This operation is necessary and of the utmost importance due to the difference at many levels between the two employed receiving units which are devoted to the recollection of total and orthogonal optical power. In this regard, the main purpose of this section of the project is the study of the evolution of calibration profiles, analyzing the stability of the calibration constant and seeking to find how external environmental parameter may affect the results of such procedures.

The final section of this work is dedicated to the validation of the products obtained by the measurements performed with this new channel. To do so, in Chapter 5, the illustrations of the most common atmospheric phenomena and their correspondent depolarization ratio profiles are shown and described together with a comparison with the results of another co-located lidar system.

Chapter 2

The UPC lidar system and the new depolarization channel at 532 nm

2.1: The Lidar system

2.1.1: LIDAR equation

To better understand how the optical properties of aerosols can be evaluated, it is necessary to start with the LIDAR equation ^[7]. Once subtracted the background signal, the expression of the instantaneous received optical signal at a given time writes:

$$S_r(R) = \frac{U \cdot O(R) \cdot \beta(R)}{R^2} e^{-2 \int_0^R \alpha(x) dx}$$

Where U is the so-called system factor. Such a term describes all the height-independent parameters of the system. In particular it is defined as:

$$U = A_r P_o \frac{c \cdot \tau}{2}$$

A_r is the effective telescope area, P_o and τ are the average power and the duration of the emitted pulses respectively.

The function $O(R)$ is the so-called *Overlap factor*, an important parameter which describes the overlap between the laser beam and the *Field of View (FOV)* of the receiving telescope.

R is the range traveled by the light and finally α and β are the so-called extinction and volume backscattering coefficient respectively.

The volume backscattering coefficient β is a measure of the amount of energy per unit solid

angle that is scattered backwards to the source. It is defined as *volume* backscattering coefficient because it depends on both atmospheric particles and molecules [4].
So, in the most general case:

$$\beta = \beta_m + \beta_p$$

It has dimension $m^{-1}sr^{-1}$.

The formula

$$e^{-2 \int_0^R \alpha(x) dx}$$

is the expressions of the fraction of transmitted energy during the path (forward and backward). It depends on the extinction ratio α which represents the reduction factor per unit length of the flux of energy. α has dimension m^{-1} .

Of course, while the former parameter simply depends on scattering phenomena (elastic scattering, in the case under analysis) the latter depends on both absorption and scattering phenomena.

Both parameters are height-dependent because the properties and the quantity of the particles change along the distance R .

In the Lidar equation, α and β are the unknowns of the system. To solve the lidar equation, particular inversion algorithms are needed.

In the case of the elastic scattering, the inversion is performed by means of the so-called Klett-Fernald method [8]. In such a method, the ratio between extinction and backscattering coefficient is assumed to be known. This parameter is also called *Lidar Ratio* and it is defined as follows:

$$L_r(R) = \frac{\alpha_p(R)}{\beta_p(R)}$$

The most frequent way of writing the solution of the Klett-Fernald method is:

$$\beta(R) = \frac{RCS(R) \cdot T(R, r_0)}{\frac{RCS(r_0)}{\beta(r_0)} - 2 \int_{r_0}^R L_r(x) \cdot RCS(x) \cdot T(x, r_0) dx}$$

Where

$$L_r^{\text{mol}} = \frac{\alpha_m(R)}{\beta_m(R)} = \frac{8\pi}{3} \text{ sr}$$

$$T(x, r_0) = e^{-2 \int_{r_0}^x [L_r(z) - L_r^{\text{mol}}] \cdot \beta_m(z) dz}$$

RCS is the range corrected signal, usually defined as

$$\text{RCS}(R) = S_r(R) \cdot R^2$$

and r_0 is the reference height chosen so to have a particle backscatter coefficient negligible with respect to the molecular one. This usually happens in the higher part of the troposphere.

As previously mentioned, one useful parameter to be measured is the depolarization rate of reflected light. Such a value, which gives important information about the shape of the encountered particle, is simply evaluated as the ratio between orthogonal and parallel power component of the backscatter coefficient^[4], namely:

$$\delta V = \frac{\beta_{\perp}}{\beta_{\parallel}}$$

The way one can evaluate these two component is by means of polarizer filters placed in front of the detectors and properly rotated according to the desired polarization direction. As it is defined, the depolarization ratio is a *volume depolarization ratio* since the backscattering coefficient depends on both molecules and aerosols. In this sense, δV measures an average of the depolarization of the two species. To evaluate the depolarization caused only by particles, it is necessary to assess such a ratio considering only the orthogonal and parallel backscatter coefficient related to the particles. This parameter is named *Particle depolarization ratio* and it is defined^[4] as follows:

$$\delta^P = \frac{\beta_{\perp}^P}{\beta_{\parallel}^P}$$

Even though δ^P can outline more precisely the aerosol species, a particle characterization made only with such a parameter would not be fully reliable either. In fact, the combination of other intensive aerosol parameters (which do not depend on aerosol quantity) is needed.

Among them is the Ångström exponent and the lidar ratio, just to mention a few [11]. In fig 2.5 an example of aerosol typing is shown.

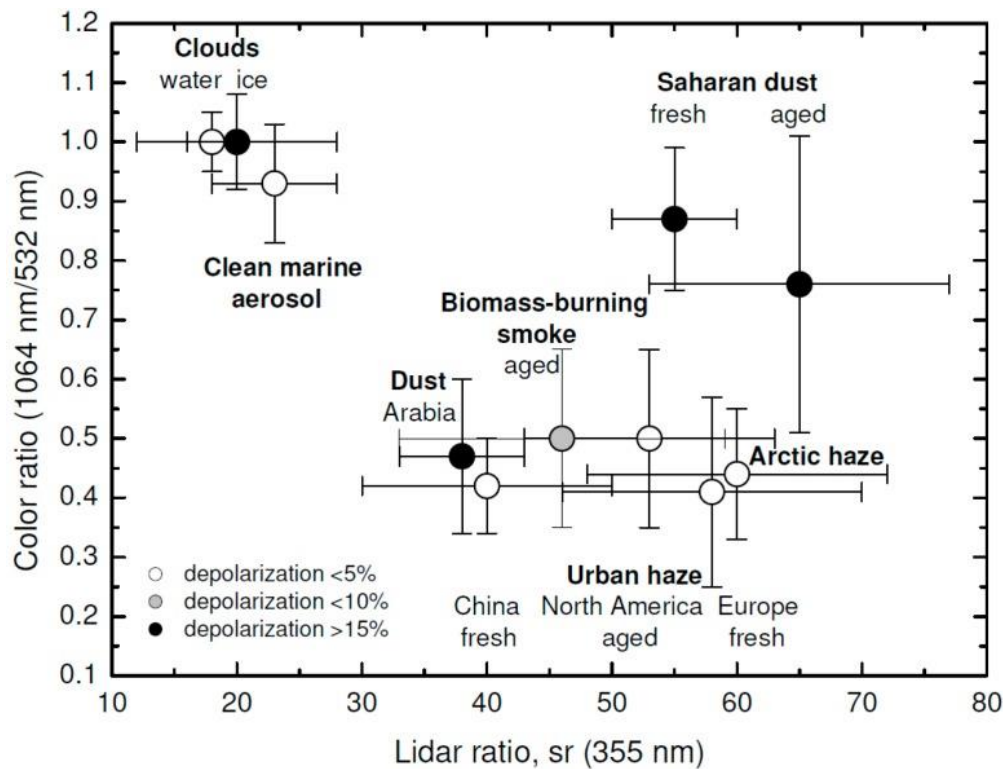


fig 2.1

Example of aerosol characterization taken from U. Wandinger et al [12].

The combination of Lidar ratio, Colour ratio and particle depolarization ratio is what allows a reliable typing of aerosol species

2.1.2: UPC Lidar system description

The Lidar system under analysis at the Remote-Sensing Lab at UPC in Barcelona [9] consists of a set of sub-systems composed of a laser responsible of the sensing light emission, a couple of telescopes which collect the backscattered light and a receiving unit that transmits and processes the acquired information.

The employed laser is a Quantel Brilliant Q-switched Nd:YAG which emits at three different wavelengths: 1064 (near-Infrared), 532 (visible) and 355 (UV) nm. The repetition rate of this laser is equal to 20 Hz, emitting at typical average energy of 360 mJ/pulse. Such a rate allows to have 1200 laser shots in an acquisition of 1 min time averages. Next to the Laser, a Schmidt-Cassegrain telescope with a diameter of 14 inches (35.545 cm) is used to collect the return signal. Once the signal has entered the telescope, at its bottom is reflected onto a 45° inclined mirror which gets it transmitted, thanks to a fibre bundle, to a 6-channel polychromator.

Fig 2.1 illustrates the main components of the system.

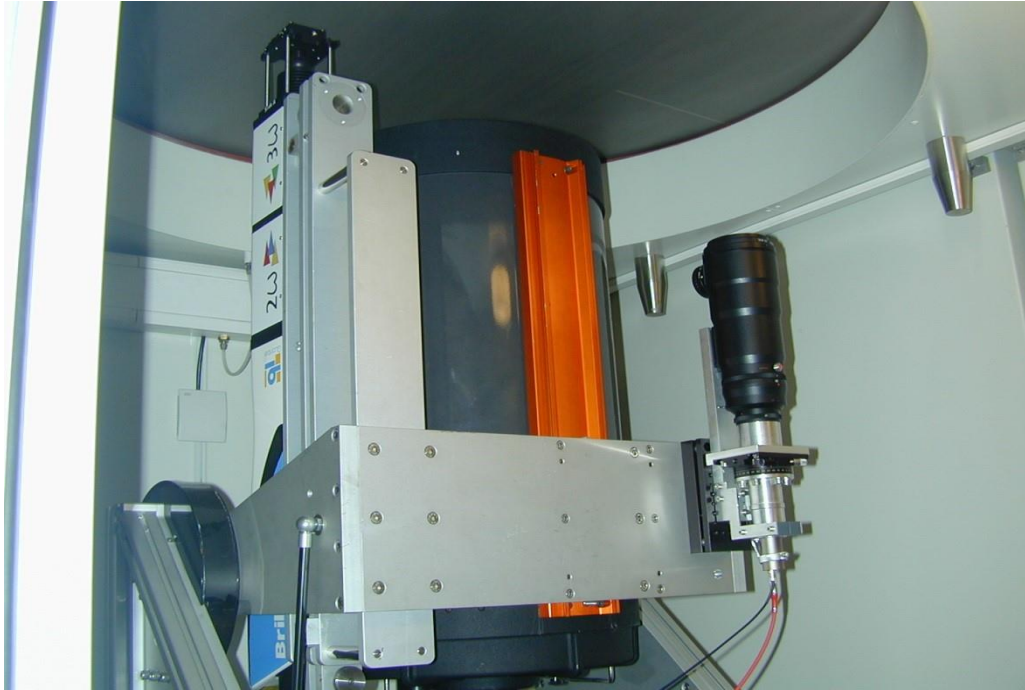


fig 2.1a

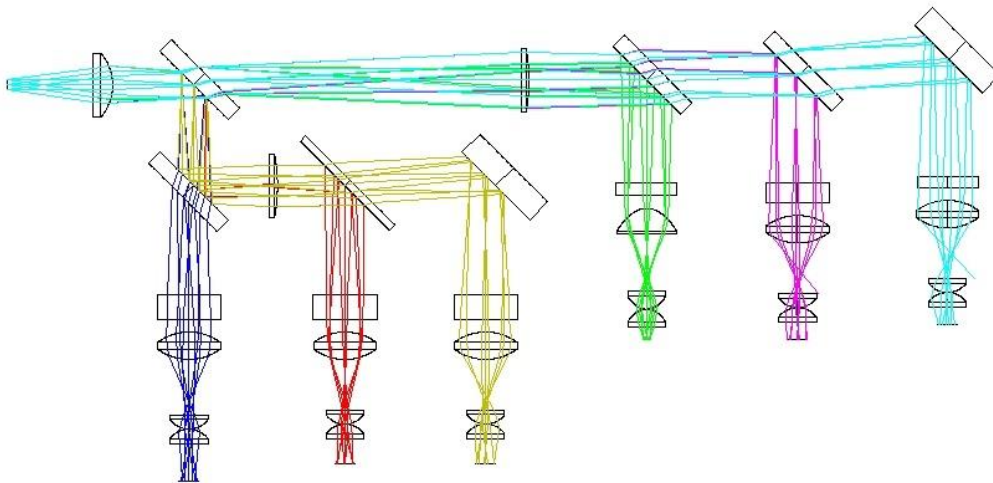


fig 2.1b

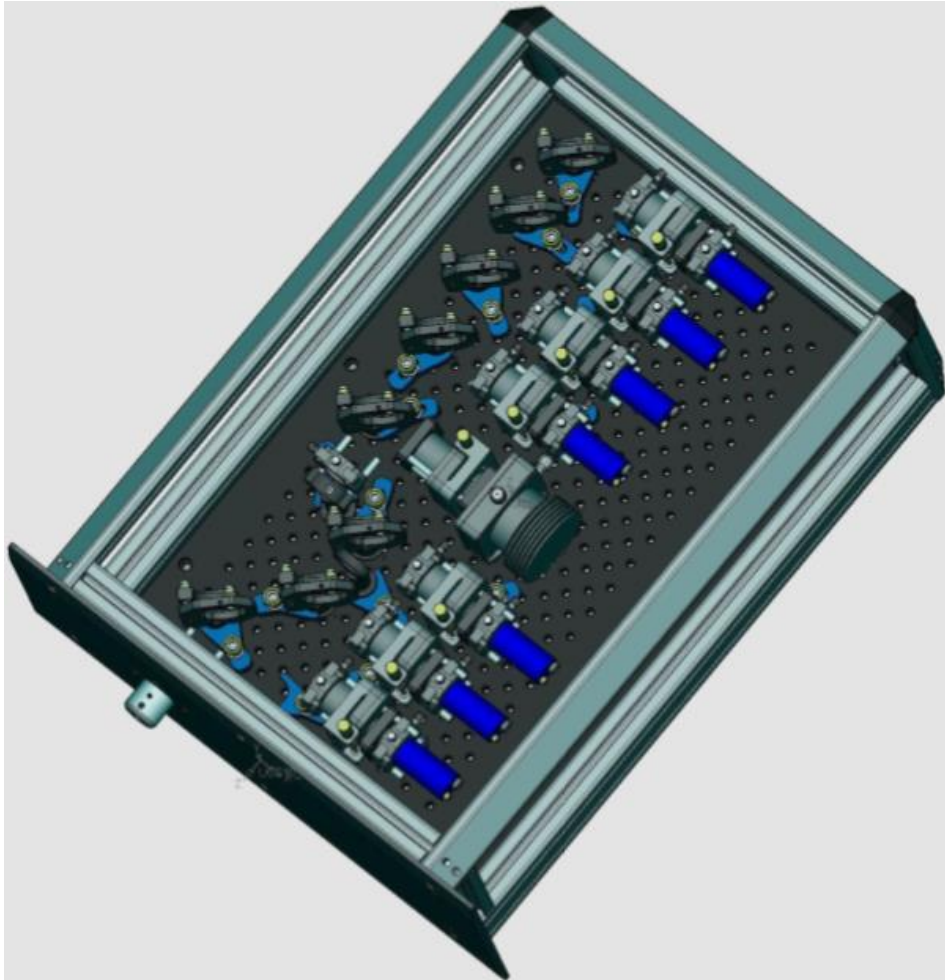


fig 2.1c

2.1a *Picture of the complete system. In the middle is the main telescope. On the right the auxiliary one, while on the left is the Q-switched laser.*

2.1b *Sketch of the Polychromator: input light coming from the fibre bundle, on top left, encounters a set of dichroic filters, lenses and mirrors which split it in 6 different channels and bring them to the Photomultipliers (PMT)*

In fig 2.1c the same polychromator is represented on AutoCAD

The advantage of the fibre bundle is that it depolarizes the incoming light in such a way that the light at its output is nearly totally unpolarized, and thus the effect of the attenuation due to the optical components in the polychromator can be neglected.

There, the optical separation is made at six wavelengths: three elastic (1064, 532 and 355 nm) and three inelastic (387, 407, 607 nm) wavelengths. In addition to the three emitted wavelengths in fact, Raman-shifted echoes are also detected. Such signals are caused by the presence of Nitrogen molecules (387 and 607 nm) and of water vapour (407 nm). Raman signals are typically four orders of magnitude weaker than the elastic ones. For this reason, once converted into electric signals, they are usually amplified with respect to the others.

2.2: The new depolarization channel at 532 nm

2.2.1 Introduction

A new depolarization channel at 532 nm of the UPC lidar system was developed in 2015/2016 and the first signals were acquired on 17/03/2016.

The setup was originally suggested by E. Calvo ^[2] and can be seen depicted in fig 2.2

It employs two independent telescopes: the already present large telescope, which collects the total backscattered signal and a new, smaller telescope which collects the signal with a polarization perpendicular to the one of the emitted light.

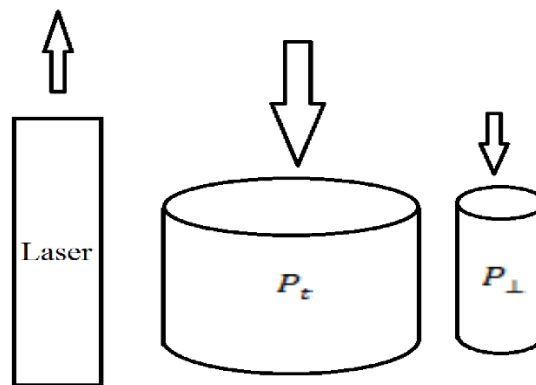


fig 2.2

Schematic of the emission and reception setup

The choice to develop a depolarization channel employing an extra telescope was considered the best option since adding other mechanical components to the main telescope, to create another 532 nm channel in it, was merely impossible due to the lack of space. This schematic, shown in fig 2.1, simply requires a new telephoto lens having a diameter smaller than the first telescope. In fact, since no optical filtering is necessary apart from the interferential filter at 532 nm, the Signal to Noise Ratio computation ^[2] gave, as a result, a similar value in the two branches having just a 7 cm diameter lens in the new telescope (much smaller compared to the 36 cm of the main telescope).

In order to collect the orthogonal component of backscattered signal, besides the telephoto lens, a polarizer filter, mounted on a rotating support, is needed. Such a simple mechanical system allows, in fact, to have the polarizer aligned both in the orthogonal and parallel position with respect to the emitted light by means of a simple rotation of the device.

To quantify the amount of light depolarized by the atmospheric particles, a calibration is needed between both channels in order to compensate the differences of overlap factors,

detector gains etc. between them. A deeper description of the calibration procedure is provided in section 3.

2.2.2 Schematic and description of the optical components

The new optical channel consists of a sequence of components properly placed after the telephoto lens, which acts as a telescope. Their arrangement is shown in fig 2.3 and their main characteristics are listed in Tab 2.1

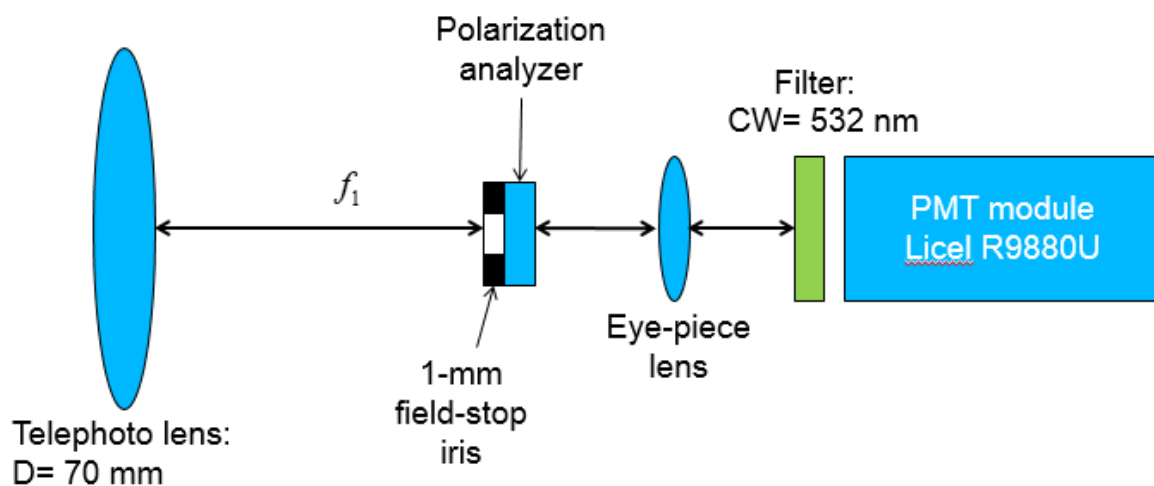


fig 2.3

*Overall layout of the optical channel.
Adapted from A. Rodríguez-Gómez ^[10]*

As can be seen in the picture, after a distance equal to the focal length, the first object light encounters on its path is the **Field-stop Iris**. This simple device basically consists of a 1mm thick Aluminium layer where a 1mm diameter aperture was drilled. This tiny pin-hole allows a very small cone angle of rays to get through. The smaller is the portion of recollected rays, the more collimated they are, and this can grant a good enhancement of the quality of the image obtained.

The dimension of the pupil diameter is directly connected to the FOV of the system, namely, the portion of solid angle which contributes to the detection.

Considering the Telephoto lens rear focal length together with the diameter of the pupil, applying some simple goniometry one can get:

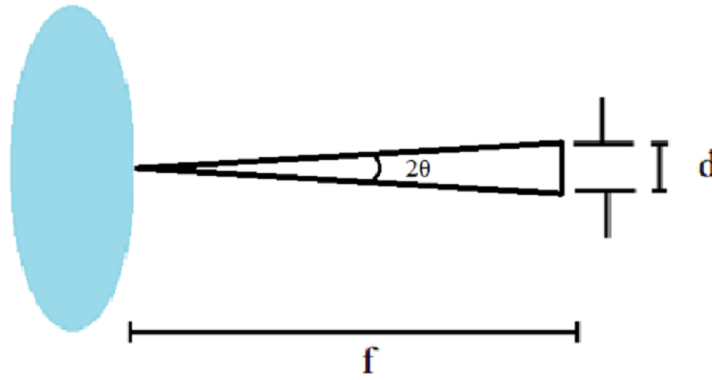


fig 2.4
Schematic of FOV computation

$$2\theta = \tan\left(\frac{d}{f}\right) = \frac{1\text{mm}}{300\text{mm}} = 3.3 \text{ mrad}$$

The choice to have such a small value of FOV is related to the necessity of having a rather small amount of incoming light rays avoiding, as much as possible, the contamination of the noisy background radiation. However, such a value was designed considering all the components of the channel together, especially the spot diameter of the final useful device, the last element of the chain: the photodetector.

ELEMENT	BRAND	MODEL	MATERIAL	DIAMETER (mm)	THICKNESS (mm)
IRIS	/	/	Aluminium	1	1
Polarizer	Edmund Optics	Linear Plastic	PMMA	25.4	2.2
Eye-Piece Lens	Edmund Optics	DCX Lens	N-BK7	25	5.3
Interf. Filter	BARR Associates	8M848	N-BK7	25.4	11

Tab 2.1
List of the optical components and key features

After the Iris, the second element forming part of the channel is the **Linear Polarizer**. Such a device is necessary to have only one polarization of the backscattered light passing through, filtering out the rest. For this reason, the orientation of the polarizer must be properly set with respect to the polarization of the Laser so to have a precise orthogonality between them. This element is what actually defines the cross-channel. In fact, it should also be emphasised that such filter is mounted on top of a metal support which allows its rotation over an angle of 90°,

$\pm 45^\circ$ from its nominal position and this is crucial to perform calibration measurements, a fundamental step to retrieve polarization ratios.

The following element of this chain is the **Eye-Piece Lens**. This lens is the fundamental device by means of which it is possible to spread the rays coming from a circular hole of 1 mm in diameter onto the bigger surface of the Photomultiplier (PMT).

To do so, the eye-piece lens is placed at a distance from the diaphragm equivalent to its focal length. In other words, its job is to recollect divergent rays and to map them, collimated, on the surface of the PMT.

Of course, the diameter of such lens must comply with the dimensions of the other components (1 inch) while its thickness slightly exceeds 5 mm.

The last but one device of this channel is the **Interferential Filter**. This element is needed because up to this point the whole spectrum of frequencies has reached this surface but the goal of the system is to isolate only the 532 nm wavelength component and to compare it with the total power (at the same frequency) impinging onto the devoted channel belonging to the big telescope. Very high selectivity is required; therefore, the characteristics of such bandpass filter shall grant very high spectral purity and very low losses. For this system, a Barr Associates Interferential Filter was chosen, centred in 532 nm of wavelength with a bandwidth of 0.5 nm.

Lastly, the PMT can be found. The role of the photomultiplier is to convert the impinging light in an electric signal which is measured and then processed. This device has a circular active surface of 8 mm in diameter and it is important to exploit it completely. In fact, having a light spot bigger than this surface would imply a loss of information as not all the incoming rays could be actively measured while, on the contrary, a smaller focused light beam eventually could damage the photodetector which preferably works with a uniformly distributed light beam on it ^[24].

- **2.2.3 δV and δP retrieval with this configuration**

Given the structure description, it is now possible to conduct an in-depth analysis on how it is possible to retrieve the two important parameters δV and δP with such a configuration. For this purpose, it may be useful to recall the definition of δV :

$$\delta V = \frac{\beta_{\perp}}{\beta_{\parallel}}$$

Which under given circumstances can be written as

$$\delta V = \frac{P_{\perp}}{P_{\parallel}}$$

Since this system does not measure directly P_{\parallel} , it needs to be reconstructed. In this regard, two considerations must be made: first of all, as previously stated, the depolarization channel is indeed able to provide an evaluation of the orthogonal component while the total channel only provides the total power;

Secondly, the power component useful to get that ratio is not exactly the raw signal which is measured. The signal which is obtained after a measurement include several other parameters which basically give a footprint of the channel itself, to be more specific, the following equations describe the acquired signals:

$$S_{\text{tot}}(R) = V_{\text{tot}}(R) \cdot P_{\text{tot}}(R)$$

$$S_{\text{dep}}(90^{\circ}, R) = V_{\text{dep}}(R) \cdot P_{\perp}(R)$$

So, as can be seen, the incoming signals are expressions of the total and orthogonal power respectively, but they are weighted by another factor: the *channel responsivity* ^[4].

Such a factor considers the numerous differences of the two involved channels such as, just to mention a few, the difference in optical path, different set of lenses and filters induce different signal attenuation, the difference of the FOV, indeed the big channel has a front lens which is five-times bigger (in diameter) than the one of the small telescope, difference in the PMT responsivity, because also the electronic involved is different, etc...

Taking the ratio of the two previous signals, one finds the first important product which is called *Depolarization Observable*:

$$\delta^*(90^{\circ}, R) = \frac{S_{\text{dep}}(90^{\circ}, R)}{S_{\text{tot}}(90^{\circ}, R)} = \frac{V_{\text{dep}}(R) \cdot P_{\perp}(R)}{V_{\text{tot}}(R) \cdot P_{\text{tot}}(R)}$$

Together with it, one should also consider the ratio of the two channel responsivities, fundamental parameter which is derived practically with a calibration measurement:

$$V^*(R) = \frac{V_{\text{dep}}(R)}{V_{\text{tot}}(R)}$$

This last parameter is called System Channel Ratio.

Once these parameters are known, the way to obtain the volume depolarization ratio is just a matter of working them properly together. For this reason, it is important to remind that the evaluation of the parallel component must be an indirect retrieval, since only total and crossed components are obtainable from the two systems.

As a result, one gets:

$$\delta V = \frac{P_{\perp}}{P_{\parallel}} = \frac{P_{\perp}}{P_{\text{tot}} - P_{\perp}} = \frac{\delta^*(90^{\circ}, R)}{V^*(R) - \delta^*(90^{\circ}, R)}$$

So, in conclusion, thanks to a simple mathematical rearrangement, one can get the volume depolarization ratio simply working out the *Depolarization Observable*, the ratio of raw input signals obtained from a measurement, together with the *System Channel Ratio*, whose derivation is deeply analysed in chapter 4.

This is the first depolarization ratio which is important to evaluate but, as it is, the evaluation of only this parameter leads to an incomplete analysis of the atmospheric aerosols because, from a quantitative point of view, δV represents an average between the volume depolarization produced both by molecules and particles, each one weighted by the backscatter they produce.

Even considering, as a first approximation, that the numerator only depends on the presence of the aerosol, it would not be possible to distinguish if a certain depolarization value is due to a high number of low-depolarizing particles or a small number of highly-depolarizing ones.

It is to say, measuring only the volume depolarization ratio can give only a quantitative description of depolarizing particles but not a qualitative one.

To better understand the nature of the encountered particles, one further step must be made, and that is the evaluation of the *Particle Depolarization Ratio*.

As with the Volume Depolarization ratio, also the Particle Depolarization ratio is retrieved taking the ratio of the orthogonal and parallel backscatter coefficients:

$$\delta^p = \frac{\beta_{\perp}^p}{\beta_{\parallel}^p}$$

Which under given circumstances can be written as

$$\delta^p = \frac{P_{\perp}^p}{P_{\parallel}^p}$$

However, in this case, the effect of particles is the only one considered, as though the effect of molecules has been removed from the weighted average mentioned above. Such a retrieval is not as easy as for the case of the volume depolarization ratio for an inversion process is necessary to separate particle backscatter coefficient to the molecule one. Putting together the expression of the total backscattered power and the Volume Depolarization ratio one gets [4].

$$\delta^p = \frac{[1 + \delta^m]\delta^v(R) \cdot \rho - [1 + \delta^v(R)]\delta^m}{[1 + \delta^m] \cdot \rho - [1 + \delta^v(R)]}$$

where δ^m and ρ are the molecular depolarization ratio and the backscatter ratio respectively and are defined as:

$$\delta^m = \frac{\beta_{\perp}^m}{\beta_{\parallel}^m} \qquad \rho = \frac{\beta}{\beta^m} = \frac{\beta^m + \beta^p}{\beta^m}$$

Concerning the molecular depolarization ratio, its value is calculated with rather high accuracy, however in this case, although it is height-dependent, considering its dependence on the filter bandwidth. According to Berhendt [25], it is possible to assess that, employing a filter with a FWHM equal to 0.5 nm, the molecular depolarization ratio value is almost constant around 0.004 [25]. Instead, as far as the backscatter ratio is concerned, that is the value that must be obtained from the total power signal through the already mentioned inversion process. As it is, lidar polarization technique can be considered solid and reliable thanks to a mathematical structure relatively easy. However, it is subject to many systematic errors (sometimes very difficult to assess and reduce with statistical techniques) which significantly affect the results.

The error analysis and its propagation is illustrated in Appendix A

Chapter 3

Optical characterization of the new depolarization channel at 532 nm

3.1: The TAIR-3S Telephoto lens

The additional telescope used to collect the new depolarization channel is in fact a telephoto lens of 70-mm diameter, model TAIR-3S. Prior to the characterization of the overall channel, some investigations about the telephoto lens were made in order to properly characterize it.

3.1.1 Introduction

TAIR-3S is a Russian telescope first made in 1955. Unfortunately, very little is known about it. Some information ^[13] allowed to find the schematic of the telephoto as a set of three lenses, sketched in fig 3.1.

L1 and L2 are respectively a bi-convex and a concave-plane lens. Together they form a convergent achromatic doublet. The third lens L3, a meniscus, is, on the contrary, a diverging lens whose main task is to enlarge the effective focal length of the device. The main parameters of such device consist in the lenses thickness, radius of curvature, diameter and their inter-distances.

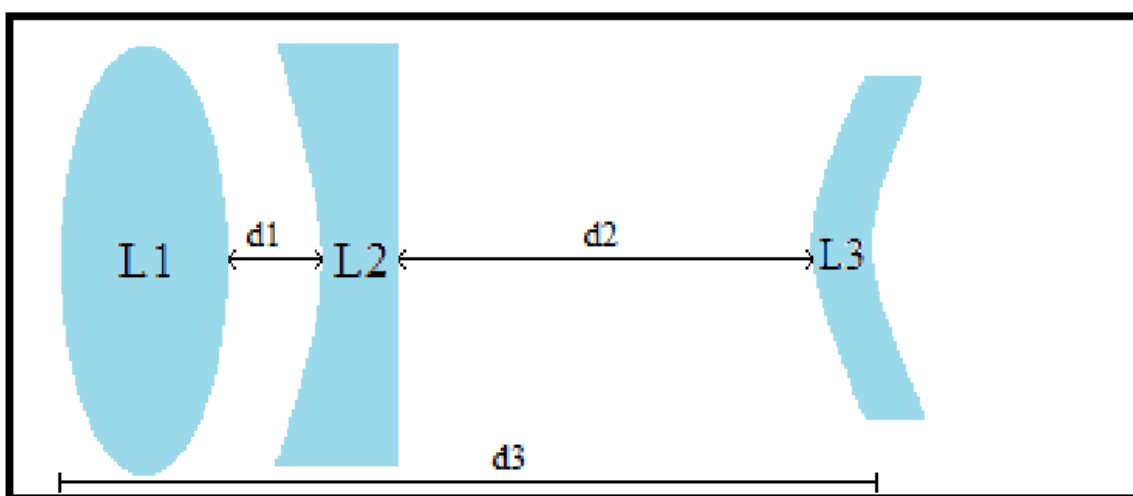


fig 3.1
Sketch of the TAIR-3S set of lenses

The known parameters of the TAIR-3S telephoto are listed in Table 3.1. For each lens, the following parameters are shown: Diameter, Radius of curvature of first and second surface, thickness and distance with respect to the subsequent surface.

Two approaches based on ZEMAX software were considered to approximate the unknown physical parameter of the telephoto: a ***trial-and-error*** method and an ***internal optimization*** method of ZEMAX.

The *trial-and-error* approach consists in adjusting intuitively the unknown physical parameters and constraining the known ones. ZEMAX allows this kind of operation simply letting the user change all the parameters concerning any surface of the system (curvature, inter-distance, material, etc.). However, due to the vast variety of possible choices, it was necessary to use a pre-existing structure with parameters similar to the wanted ones and then modify them properly.

To do this, ZEBASE was employed. ZEBASE is a ZEMAX supported database which contains a collection of lens designs with which the user can start customizing its own application.

3.1.2 Zemax procedure and results

As a starting point, the telescope objective A_019 present in ZEMAX Database ^[14] has been used. Although being slightly different, it is made of an achromatic doublet with characteristics rather similar to the actual system under analysis. Of course, the third lens, the meniscus, was missing in this pre-existent model and was intuitively customized and added to the Lens Data Editor of the software. Once the first Telephoto lens model was realized, it was easily possible to verify the goodness and reliability of its features by looking at the final spot light created when it impinged perpendicularly on the first useful surface of the system, devoted to the recollection of the rays: the diaphragm. The results, which are summarized and illustrated in Table 3.3, show a not perfectly focused light beam with a huge quantity of rays spreading all over the 1 mm diameter IRIS. The reason which explains such odd behaviour is the effect of spherical aberration. According to this phenomenon in fact, though involving rays having the same frequency, when light is described covering a path made of real lenses with spherical surfaces, the rays meet before and after the focal point depending on their initial inclination and their distance from the optical axis. On the contrary, if the lenses were ideal, one should have all the rays converging at one specific geometrical point, namely, the focal point. Such phenomenon is, of course, unavoidable since a real system is used, so the only applicable remedy is a design which seeks to minimize this effect.

Such inaccuracy was also proved by means of an additional tool which employs a custom-made MATLAB routine (see Appendix B) which evaluates optical parameters of a lens system, describing its components according to the *thick lenses theory* ^[15].

As a result, shown in Table 3.2, the optical parameters of interest turned out to be widely different from the expected ones and a further correction was needed.

To correct the previous values, an internal optimization tool provided by ZEMAX was used. This feature allows the software to run many simulations changing values related to some components of the system (selectively highlighted by the user) until it finds the best focus, it is to say the minimum diameter light spot on the target surface.

As a double check, the MATLAB routine was run with the optimized parameters giving, as a result, more coherent values (see Table 3.2).

The parameter resulting from the Zemax optimization are used to simulate the TAIR-3S Telephoto lens in the following:

LENS	PARAMETER	UNITS	KNOWN	TRIAL AND ERROR	ZEMAX OPTIMIZATION
L1	D	mm	70	70	70
	R1	mm	/	86	89.22
	R2	mm	/	-86	-86.81
	T	mm	/	20	23.22
	d1	mm	/	0.5	1.1
L2	D	mm	70	70	70
	R1	mm	/	-86	-85.56
	R2	mm	inf	inf	inf
	T	mm	/	13	15.411
	d2	mm	/	105.5	95.56
L3	D	mm	/	32	31.93
	R1	mm	/	35	389.11
	R2	mm	/	25	150.59
	T	mm	/	6	3.19
	d3	mm	145.4	145.4	139.49

Table 3.1
Physical parameters of Telephoto lenses

PARAMETER	UNITS	KNOWN	TRIAL AND ERROR (computed)	ZEMAX OPTIMIZATION (computed)
f	mm	300	344.8	303.03
f/#	(dimless)	4.5	5.2	4.58
EPD	mm	66.7	66.7	66.7
Rear vertex focal length	mm	142.34	130.34	137.79
Front vertex focal length	mm	-371.14	-581.6	-389.69

Table 3.2

Optical parameters of the Telephoto lens according to the trial-and-error approach and Zemax approximation. Such values are assessed by means of thick lens analysis. (see appendix B)

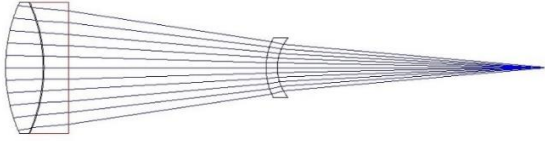
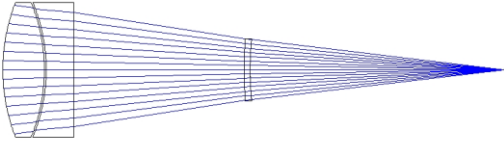
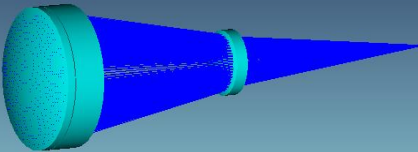
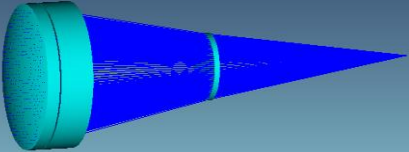
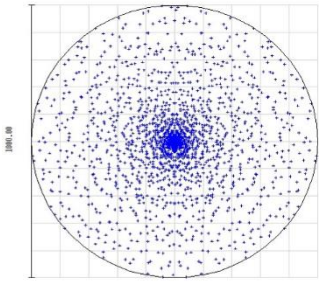
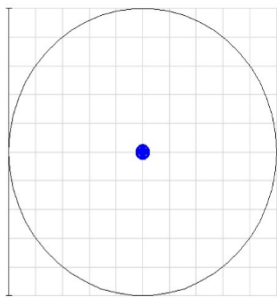
	TRIAL AND ERROR	ZEMAX OPTIMIZATION
OPTICAL LAYOUT 2D	 Layout	 Layout
OPTICAL LAYOUT 3D		
SPOT ON THE 1mm DIAPHRAGM	 Surface: 7 Diameter: 0.000 mm Spot Diagram	 Surface: 06 Diameter: 0.000 mm Spot Diagram

Table 3.3
2D-3D layouts and focused spot of TAIR-3S according to the two approaches with axial rays

3.2: Optical characterization

3.2.1 Complete analysis of the channel

Starting with the previous partial result, it was possible to complete the chain, adding all the remaining objects composing the whole optical channel. Such composed structure is depicted in fig 3.2

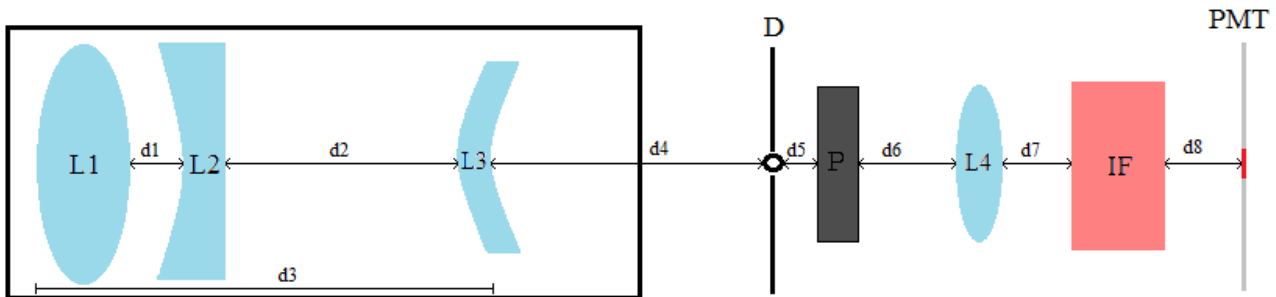


fig 3.2

Sketch of the complete optical channel

At the right distance after the last lens of the TAIR-3S is placed the diaphragm and then, following, a polarizer, an eye-piece lens (whose main task is to project the image on the whole surface of the PMT), the interference filter and finally the PMT.

The main purpose of this analysis was to rebuild on Zemax the system as it appears and check if the arrangement of its components is the one that truly grants a successful optimization of the PMT surface or possibly describe which modifications would be useful to reach it.

In Table 3.4 the key features of these objects are recalled.

OBJECT	BRAND	MODEL	MATERIAL	RADIUS OF CURVATURE (mm)	DIAMETER (mm)	THICKNESS (mm)
D			Aluminium	Inf	1	1
P	Edmund Optics	Linear Plastic	PMMA	Inf	25.4	2.2
L4	Edmund Optics	DCX Lens	N-BK7	40.42	25	5.3
IF	BARR Associates	8M848	N-BK7	Inf	25.4	11

Table 3.4
Features of the objects employed in the channel

Even though Zemax can distinguish between different materials (generally the typical ones of lenses and filters), such a parametrization was not actually needed since it showed having consequences only on the power evaluation of the rays and not on their direction, due to the attenuation such devices naturally cause.

Besides that, in the case of the polarizer, since no evaluation of the polarization sensitivity was carried, only the substrate material was indicated (PMMA) with no further description of the layers composing it.

On the contrary, concerning the interferential filter, it was possible to implement, by means of a proper Zemax Macro ^[16], the many layers (MgF₂) deposited on the top of it and check the behaviour depending on the frequencies used as input light beam.

However, Zemax also allows to use a perfectly mono-chromatic light source and, in order to keep the simulation at a simpler level, this last choice was pursued.

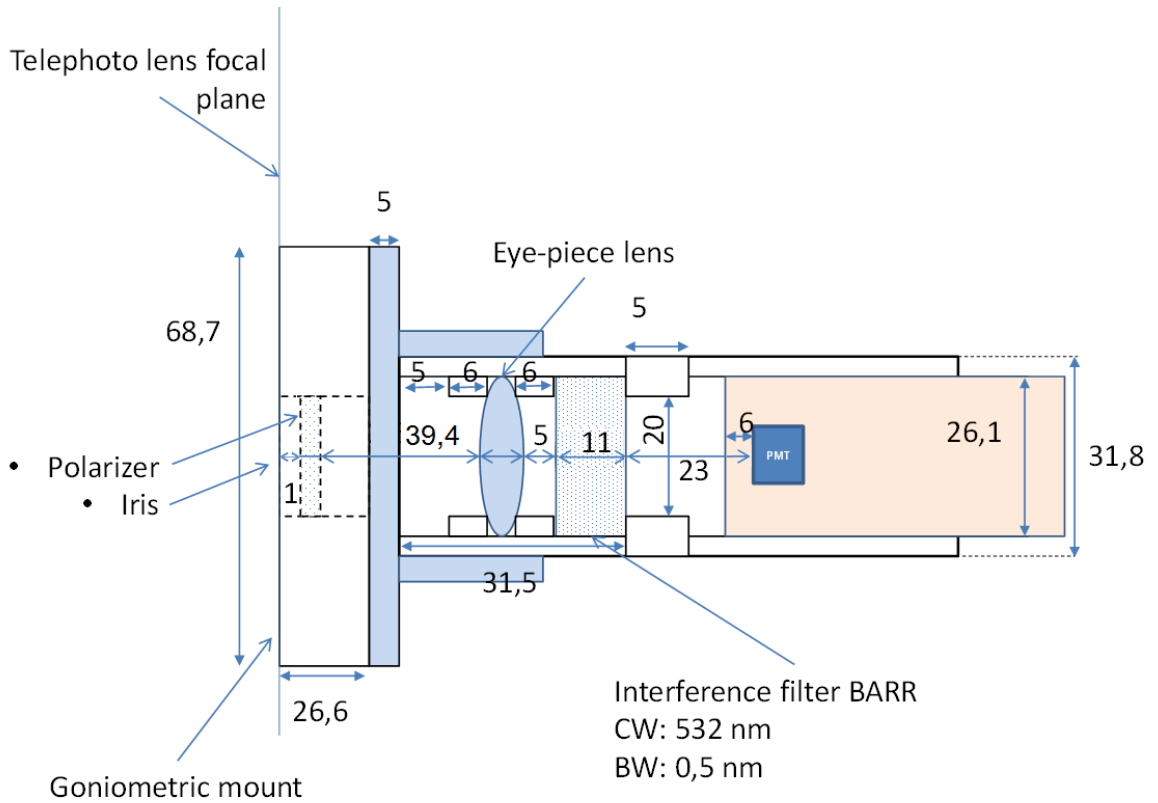


fig 3.3
Complete scheme of assembly parameters of the optical channel.
Distances are in mm

Distance	Value (mm)
d4	142.34 (original) – 138.934 (computed)
d5	1
d6	39.4
d7	5
d8	23

Table 3.5
List of distances between channel components

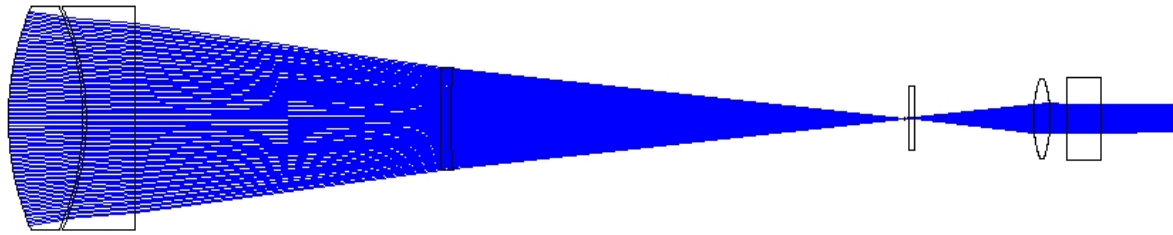


fig 3.4
2D Zemax representation of the whole channel

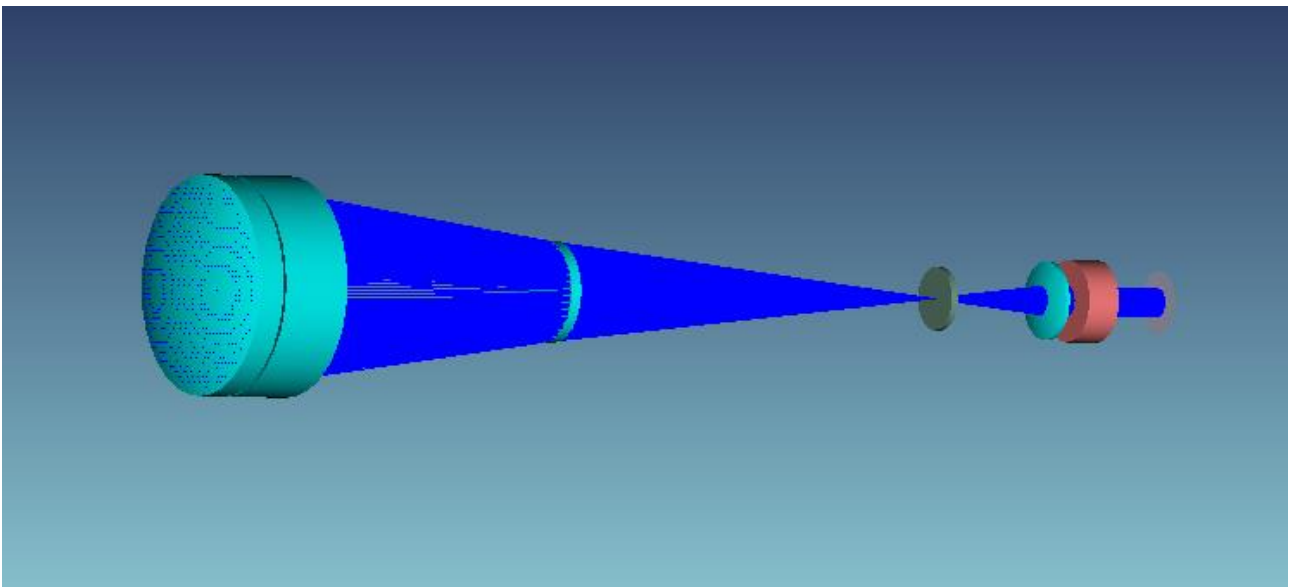


Fig 3.5
3D Zemax representation of the whole channel

3.2.2 FOV evaluation and final spot

Concerning the evaluation of the FOV, a proper way to calculate it within Zemax was not found, for this reason what is presented is a table which indicates the percentage of starting rays which impact on the final spot and the consequent diameter of the global spot as the incident angle of the light beam increases.

The numerical results are listed in Table 3.6

FOV (mrad)	% <u>oblique</u> rays reaching PMT surface	Overall Spot Diameter (mm)
1.75	99.8	8.62
2.44	90	8.76
2.85	82.1	8.78
3.14	68.4	8.8

Table 3.6

List of the percentage of rays impinging on the PMT at different angles

It is rather clear that the expected theoretical value of the FOV equal to 3.3 mrad (derived in section 2) is not reached but from a small percentage of the incoming rays, making the computed FOV having a smaller value. However, this result was to be expected. In fact, in this channel there are many contributions which cause the FOV to have a value far from the ideal one: the telephoto group composed by three real lenses (instead of an equivalent thin one) and the actual thickness of the diaphragm are just two of them.

As a result, according to this analysis, the light beam exceeds the 8 mm diameter of the Photomultiplier. This means that, with the present configuration, there is a roughly 21% of light which is missed by the PMT surface. This evaluation is made considering the value showed as GEO radius: such radius value is calculated by Zemax as the distance from the centre to the farthest ray position spotted on the final surface^[16].

Taken this radius value, the power estimation was made assuming a uniform distribution of the rays on the PMT surface.

However, it is a reasonable expectation that light rays spread unevenly on the final surface and that most of them tend to focus in the centre of the circle.

Under these assumptions, most of the power would be concentrated on the PMT surface leading to a smaller percentage of lost power.

In fig 3.6 it is possible to see a Zemax representation of PMT surface and how it is reached by normal and oblique rays

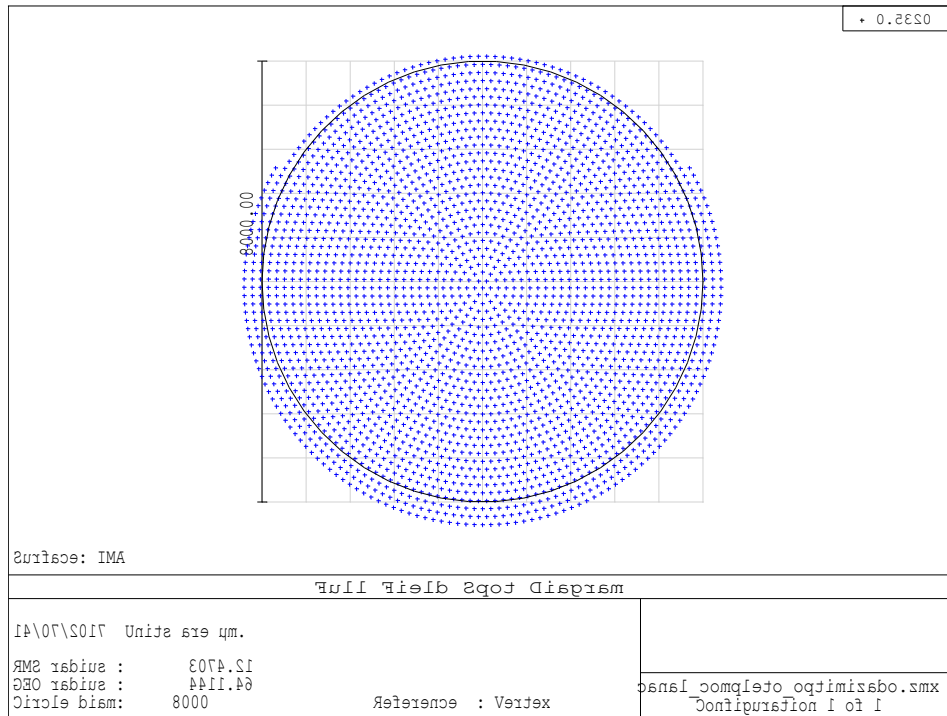


fig 3.6a

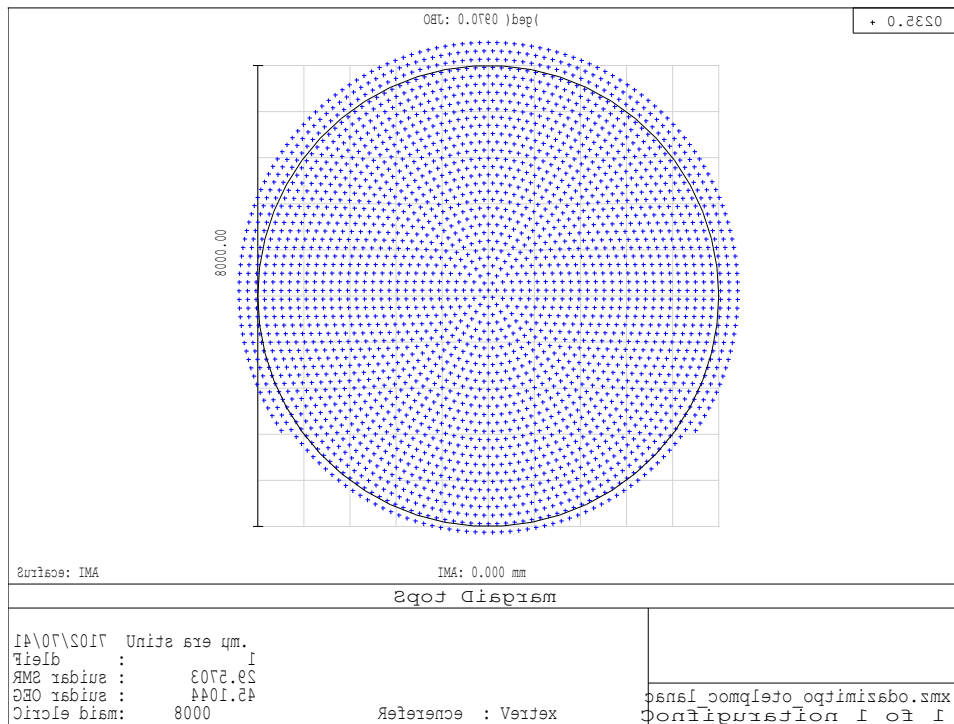


fig 3.6b

**Pictures of the PMT surface reached by the two outermost light beams
(corresponding to a total FOV of 3.14 mrad)**

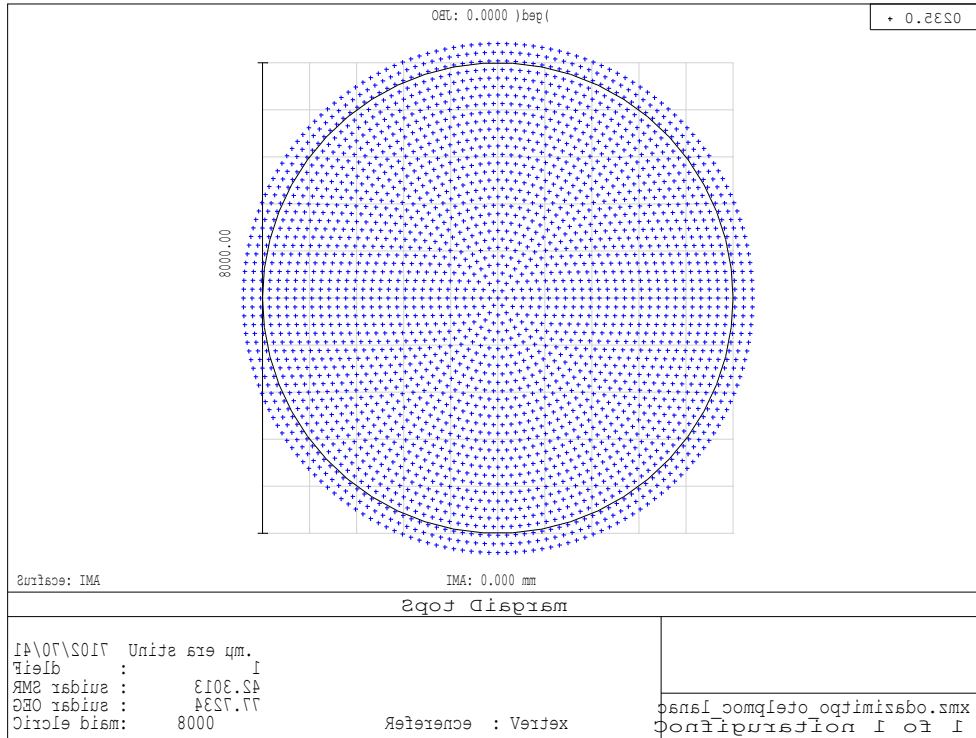


fig 3.7

Picture of the PMT surface reached by a perpendicular light beam

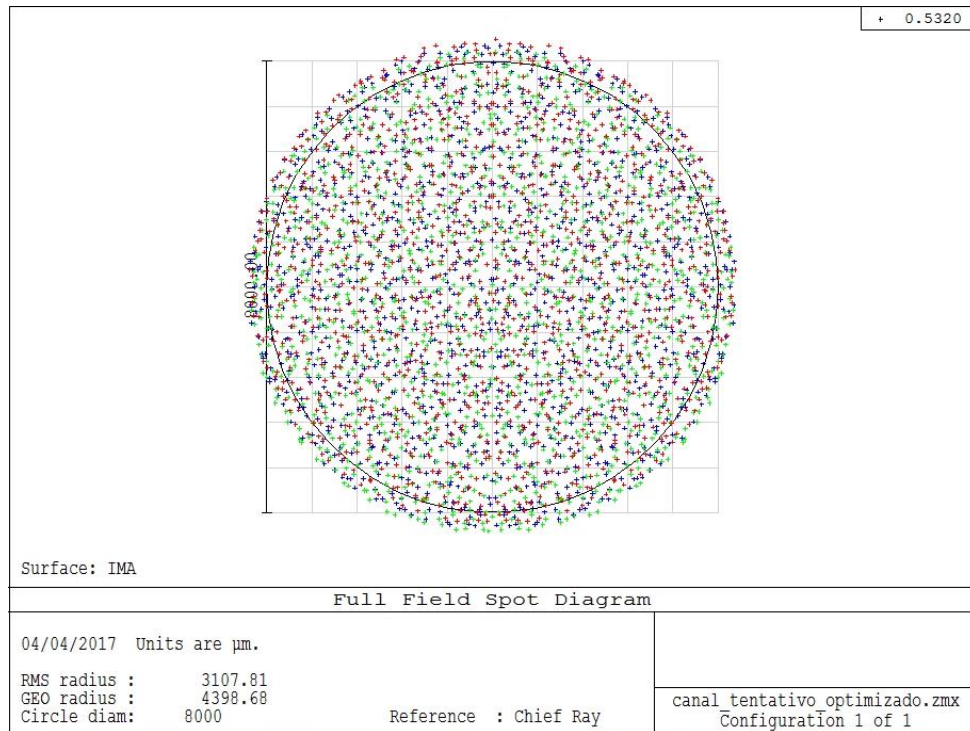


fig 3.8

Picture of the PMT surface reached by all the light beams: perpendicular and oblique ones. Blue for the perpendicular rays, red and green for -1.57 mrad and $+1.57$ mrad respectively

To avoid the loss of information acquired, it could be possible to properly displace the last objects of the channel. In fact, the eye-piece lens is a converging lens which could grant a better convergence if the PMT was placed farther from the IF filter. However, being a very small rate of convergence, a great displacement would be required and this, because of the lens-supports disposition, turned out to be impractical.

In table 3.7 are summarized the most important parameters values resulting from this optical characterization of the channel:

Parameter	Theoretical value	Computed value
FOV	3.3 mrad	2.85 mrad
Spot diameter	8 mm	8.8 mm (21% signal is lost)

Table 3.7
Summary of the results of the channel optical characterization

Chapter 4

Calibration of the new depolarization channel at 532 nm

4.1: Calibration Method

4.1.1 The System Channel Ratio retrieval

As briefly introduced in chapter 2, to get the Volume depolarization ratio is necessary to consider the *channel responsivities*. In fact, the two measured power components are weighted by this other factor which is a parametrization of the optical and electrical difference of the two channels.

Here below, the expressions of the input signals are recalled.

$$S_{\text{tot}}(R) = V_{\text{tot}}(R) \cdot P_{\text{tot}}(R) \qquad S_{\text{dep}}(90^\circ, R) = V_{\text{dep}}(R) \cdot P_{\perp}(R)$$

The system channel ratio is the definition of the ratio of the two channel responsivities and it appears in the expression of the evaluation of the Volume depolarization term.

$$\delta V = \frac{\delta^*(90^\circ, R)}{V^*(R) - \delta^*(90^\circ, R)}$$

where

$$V^*(R) = \frac{V_{\text{dep}}(R)}{V_{\text{tot}}(R)}$$

is the system channel ratio.

To evaluate this parameter a calibration procedure is needed. This is done by performing two shorter measurements in a row with the polarizer rotated with respect to its nominal position first at +45° and then at -45°, hence the need of a rotating metal support for the polarizer. The 90° difference between the two measurements was proved ^[4] to be the best solution to have error compensation over a large range of angle uncertainty values and this difference can be achieved employing a mechanical limit stop which can grant high accuracy.

Once the polarizer is displaced from its nominal position, both in the +45° and in -45° case, the depolarization channel measures the same backscattered signal as the large telescope: the total power component. By means of this, it is possible to compare the two channels in order to evaluate the ratio between their responsivities.

To do so, it is necessary to take the geometric mean of the *depolarization observable* in the two successive measurements. It is to say

$$V^*(R) = 2 \cdot \sqrt{\frac{S_{\text{dep1}}(90^\circ + 45^\circ, R)}{S_{\text{tot1}}(R)} \cdot \frac{S_{\text{dep2}}(90^\circ - 45^\circ, R)}{S_{\text{tot2}}(R)}}$$

Once this value is retrieved, it is possible to evaluate the *volume depolarization ratio*, whose formula was incomplete up to this point.

Of course, the calibration ^[17] ^[18] is a procedure which should be done as often as possible and the used values must be the closest in time to the measurement. Only under these conditions it is guaranteed that both the calibrations values and the depolarization observables are in good accordance.

4.1.2 Daytime and night-time calibrations

Employing Lidar system, two kinds of measurements with very different features are convenient ^[9]: photon counting and analog. The necessity of having two detection modes comes from the different behaviour of the system in presence of a huge background radiation (daytime measurements) or in darkness conditions (night-time measurements).

The photon counting system allows the counting of single *photon* but its channel saturates in presence of high level of background radiation. For this reason, such channels can be operated only in low light conditions.

Analog counting, instead, can be operated both during the day and the night.

The advantage of having these two types of systems is that a gluing operation is performed when dealing with both types of signals, it is to say only during night-time measurements. Such a gluing is made by combining the results of the measurements of the two acquisition systems exploiting the benefits of the two in their favourable altitude zone: in fact, at low altitude when the SNR has high values, a better description is made with the analog system while at

high altitude, being the Analog very noisy, the photon counting is to be used. An example is shown in fig 4.1a and 4.1b.

It is recommendable that a glued measurement be associated to a glued calibration, for this reason night-time calibrations are preferred to daytime because only in this case gluing operation is possible thanks to the presence of both signals.

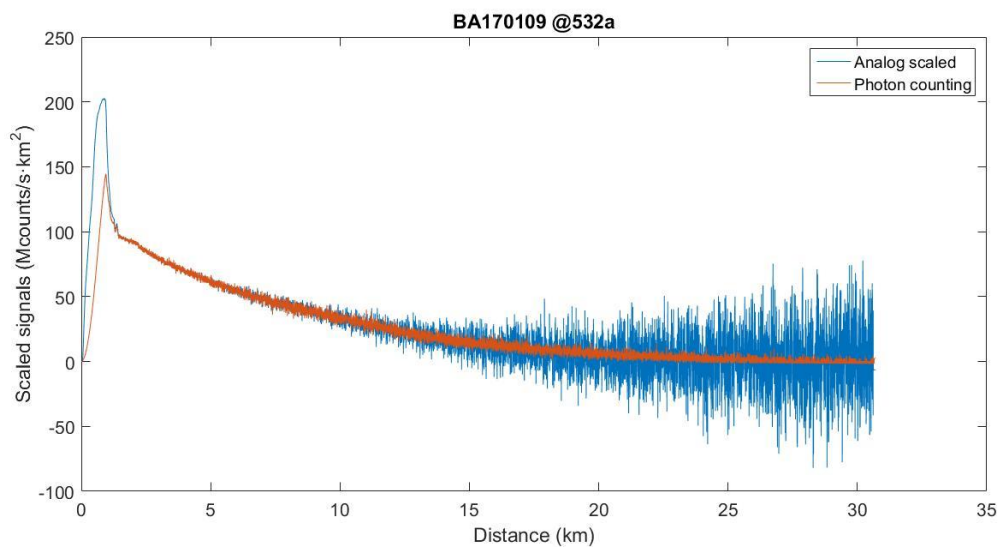


fig 4.1a

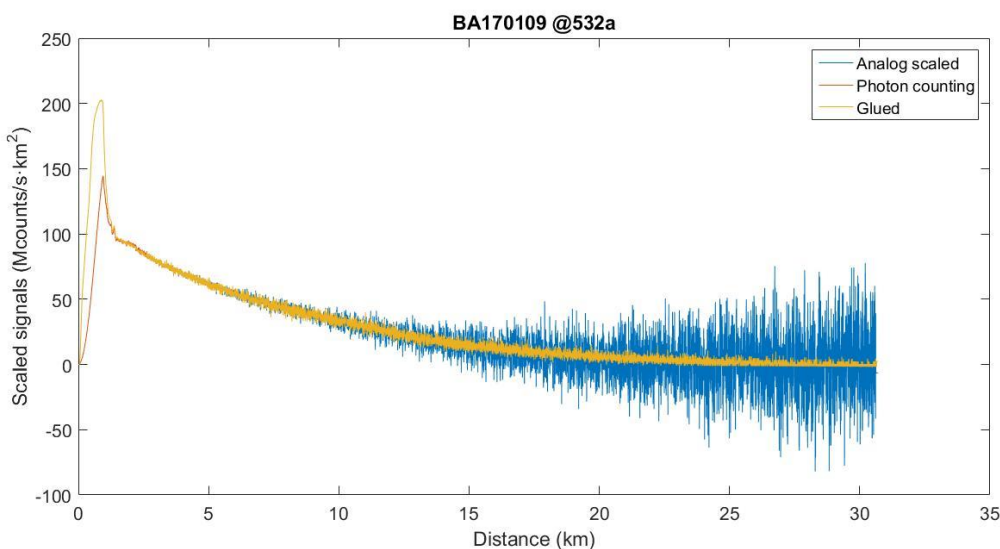


fig 4.1b

4.1a Difference between Photon-Counting (PC) and analog detection mode

4.1b Gluing between PC and analog signals. It can be seen how the gluing coincides with PC at high altitude (where analog signal is noisy) while at low altitudes it coincides with analog one

4.2: Matlab Implementation

Matlab implementation first requires the evaluation of the depolarization observable in the two cases (+45° and -45°) and then the computation of their average. In fig 4.2a such plots are shown in the case of a night-time calibration.

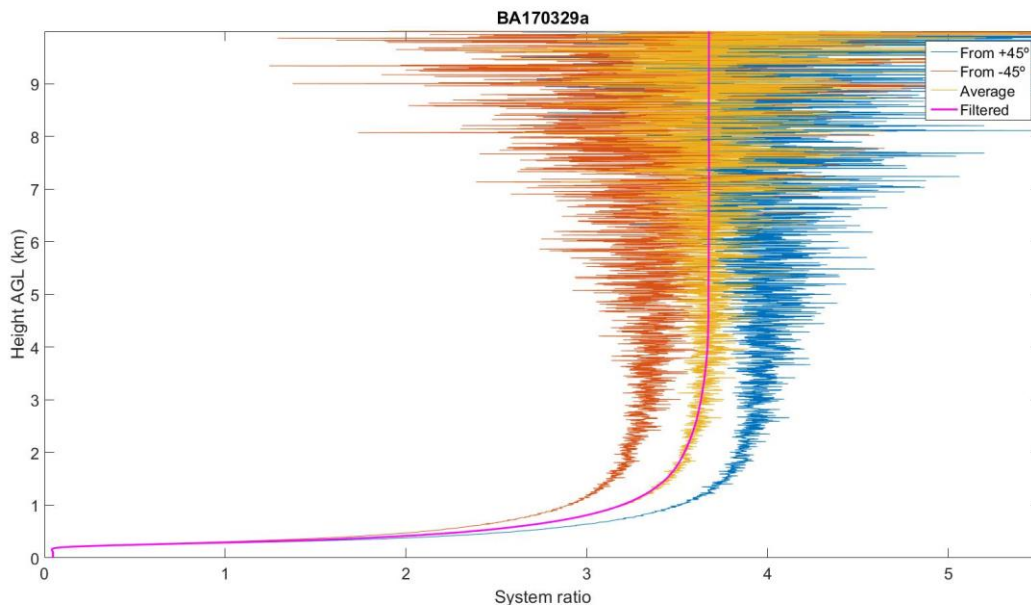


fig 4.2

4.2 Result of the average (yellow) performed between $\delta^*(90^\circ + 45^\circ)$ and $\delta^*(90^\circ - 45^\circ)$ and its smoothing (pink). The filtered pink curve is the so-called calibration vector.

The two lateral curves respectively represent the depolarization observable at +45° (blue curve) and at -45° (brown curve). Their distance shows that there is a difference in the detection for the two configurations, namely, when the polarizer is placed at +45° it collects more power. Such an asymmetry should be resolved by making a realignment of the channel in such a way to get similar detected power in the two cases. The yellow curve represents the average of the two. Due to the noise shown at high altitudes, a filtering operation is needed giving, as a result, a smoother curve (pink curve in fig 4.2). To have uniformity of the results from different calibrations, 9 km was chosen to be the maximum altitude at which the smoothing is performed and from which the same value of the system ratio is maintained. This operation is useful to compare different calibration vectors in the far range, operation which is analyzed in the next section of this chapter.

4.3: Calibration stability

4.3.1 Calibration profiles over time and error budget

A historical analysis of all the calibrations procedures performed since the beginning was needed. The purpose of such a collection of data is to describe the evolution of calibration vectors in time in order to analyze how it changed over time when certain mechanical adjustments in the systems were made.

Fig 4.3 shows how calibrations vector shape changed since the first calibration performed on 24/05/2016 until the one performed on 15/06/2017.

In the following, different approaches to study the differences between these curves are outlined.

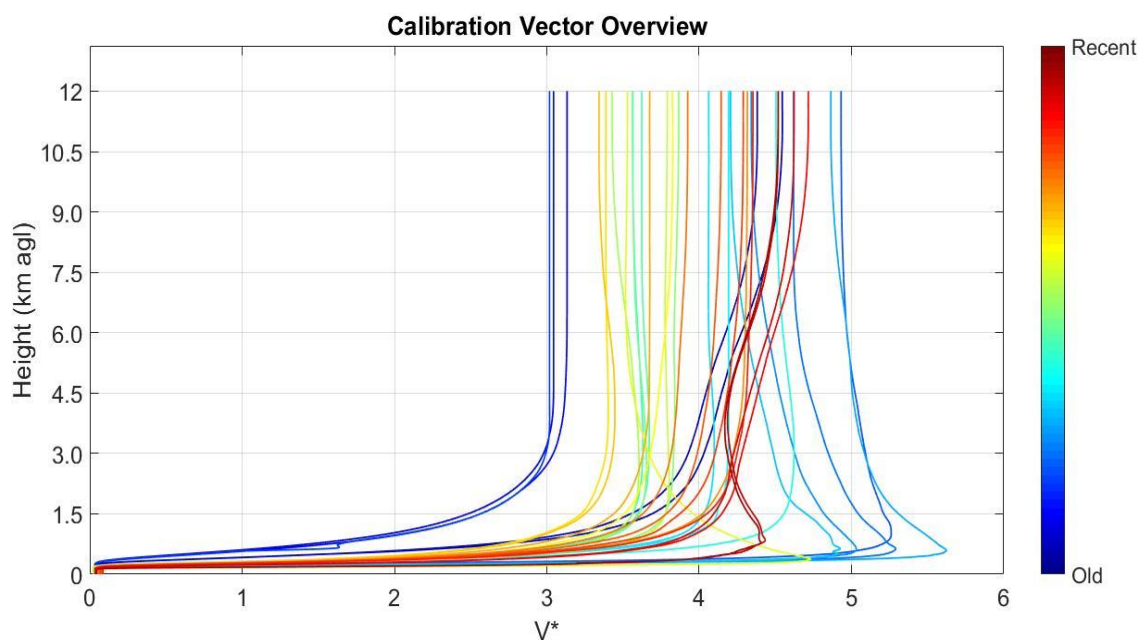


fig 4.3

Overview of all the calibrations vectors over time.

The first analysis which is done is aimed at evaluating the far range value for each calibration vector and display them all together versus time. The result is shown in fig 4.4

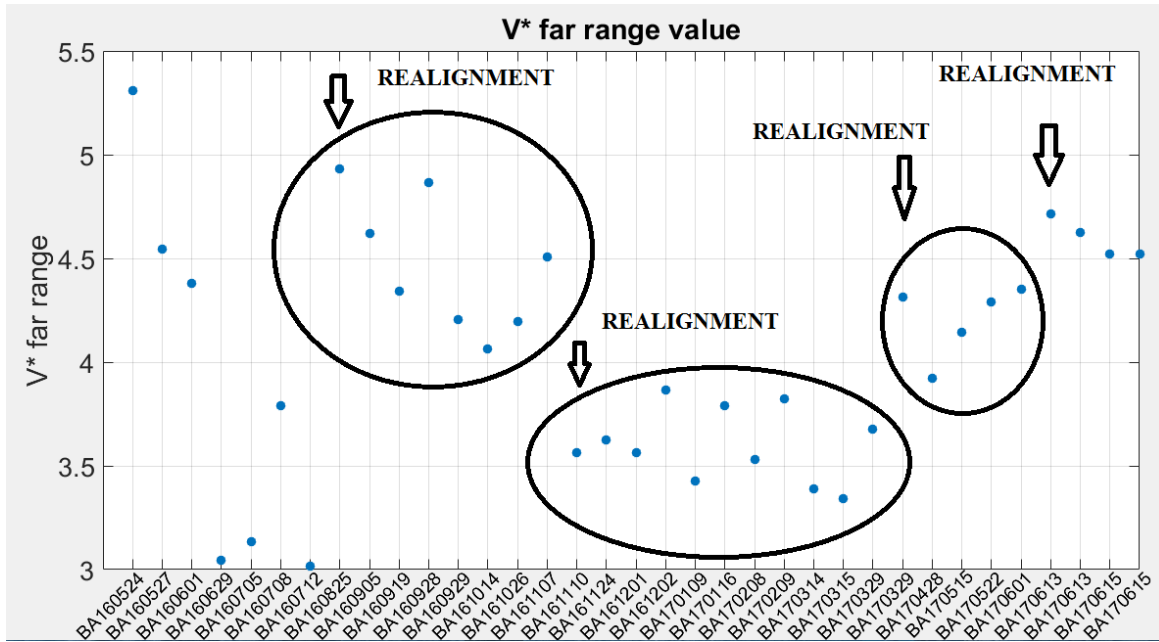


fig 4.4
Display of all calibration vector far range values over time.
Realignment dates are also highlighted.

As it can be seen, leaving out the first results, starting from the 25/08/2016, the far-range values appear to be grouped having a difference in values which stays within a $\frac{\Delta V^*}{V^*} = 10\%$.

Such a value is what has been implemented as absolute error of the system channel ratio for the computation of δV and δP error bars (see appendix A).

In fact, big variations in value can be noticed only in presence of realignments of the system. These adjustments are necessary because, over time, the depolarization channel experiences a natural displacement of its main axis with respect to the large telescope resulting in an alteration of the measured power and in the unreliability of the results.

So, when these adjustments are performed, as indicated in fig 4.4, it is reasonable to have such jumps in value.

An alternative way to evaluate the difference of the calibrations vectors over time is the so-called **Piecewise Normalized Distance**.

Such a parameter was considered ^[19] because it is a useful instrument to compare vectors over their complete range.

In this respect, the normalized distance gives an evaluation of the difference in *shape* of the vectors with respect to the last calibration.

According to the following formulas, in fact, the normalized distance between vector equal in length X_a and X_b , is defined as

$$d_{a,b}(n, m) = \sqrt{1 - \sigma_{a,b}(n, m)}$$

where

$$\sigma_{a,b}(n, m) = \frac{(\sum_{i=n}^m X_a(z_i) \cdot X_b(z_i))^2}{\sum_{i=n}^m X_a^2(z_i) \cdot \sum_{i=n}^m X_b^2(z_i)}$$

being z_i the altitude in the range (n, m) at which both vectors are evaluated.

As it can be seen in fig 4.5, each column represents a calibration vector over its complete range. However, instead of integrating over the whole range, each column pixel is the result of the evaluation of the variance σ in a smaller altitude range (10 bins \cong 37 m) so to have a higher discretization and the possibility to better compare vectors piecewise, it is to say segment by segment.

Of course, being the normalized distance evaluated with respect to the last calibration vector, in that case the result will be identically equal to 0, since the variance is $\sigma=1$.

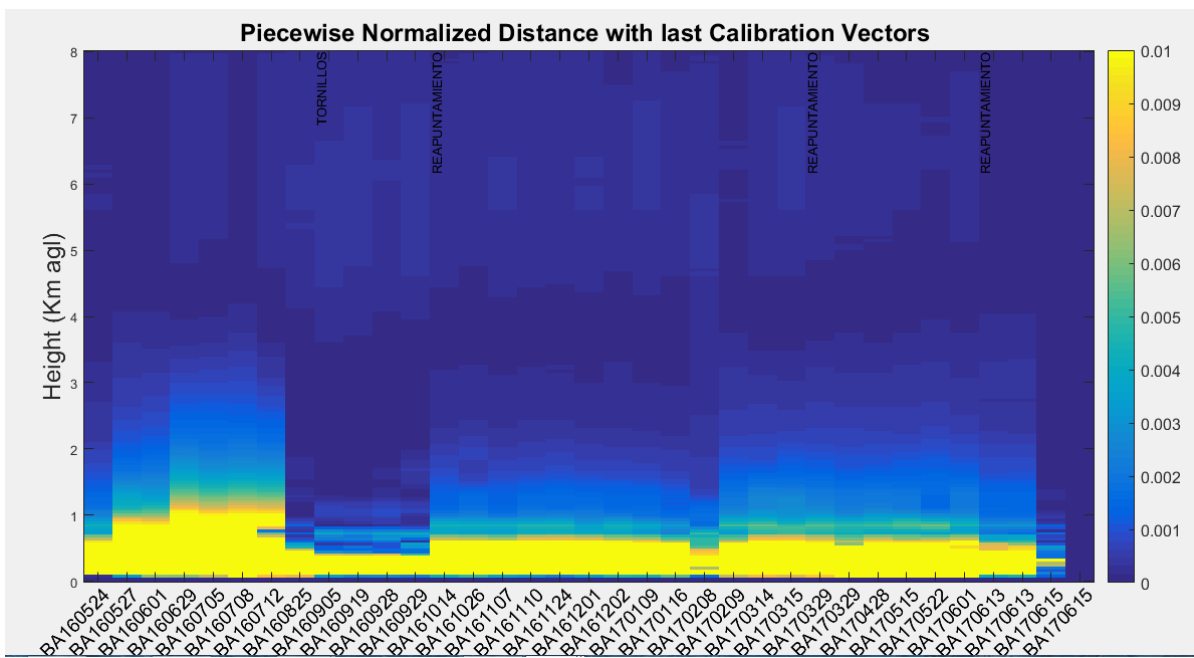


fig 4.5

Matrix representation of the piecewise normalized distance.

Once again, it is possible to see how the most significant difference between each vector and the last one stands mainly in the first 1.5 km of altitude, giving bigger values as a result. While, moving upward, one can see how the normalized distance tends to lower values meaning that vectors look alike in shape.

4.3.2 Calibration over temperature

In addition to the study of far range values over time, another type of analysis could be made: in fact, by recalling the values of the environmental temperature in correspondence of the date and hour of the calibration, it is possible to detect a dependence between far range values of calibration vector and temperature.

The results are shown in fig 4.6

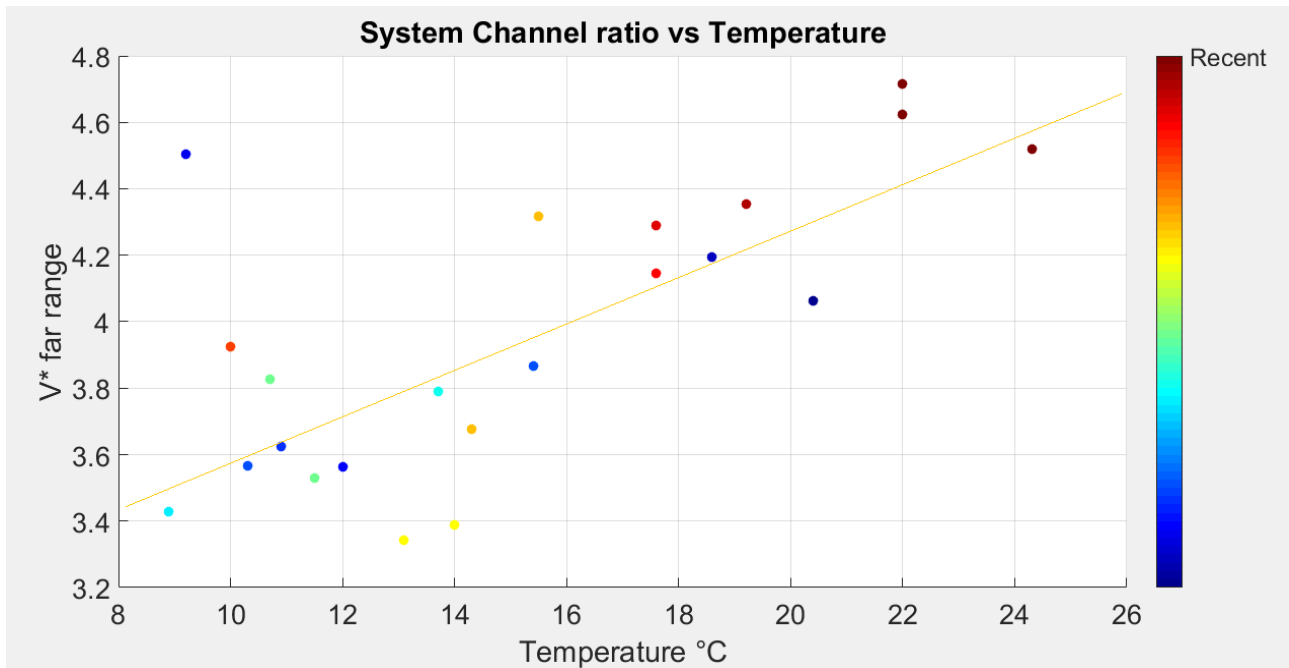


fig 4.6

Sketch of the relationship between calibration far range value and environment temperature. On the right, the colour scale distinguishes the most recent calibration values from the oldest. The yellow line is the linear best fit line.

A linear trend is noticeable, meaning that an increase in temperature modifies the system causing a growth of the system channel ratio far-range value.

Chapter 5

Retrieval of volume and particle depolarization ratios

5.1: Comparison with SCC

The first comparisons presented are between depolarization profiles both measured and processed within UPC with other profiles which, on the contrary, are processed with SCC^[22] algorithms.

SCC is a web-tool with which is possible to process data employing common algorithms and sharing a common database for every station user within EARLINET. The necessity to exploit, in a big network like EARLINET, such an instrument comes from the need to have access to high-quality data and vertical profiles which must be comprehensible to any user within EARLINET. In fact, using different retrieval approaches among different research stations eventually leads to a complete inhomogeneity of the stored data set while, thanks to the SCC, a common language between different lidar stations is achievable.

Within SCC it is possible to describe in detail the characteristics of any lidar station (different channels, detection modes, calibrations, etc...) and derive products in a completely automatic and precise way. Moreover, the possibility to adapt SCC analysis to data measured by new lidar systems or upgraded ones makes it an essential tool for EARLINET users to the point where internal algorithms will be completely replaced.

For the time being, SCC represents an excellent mean of comparison with which it is possible to evaluate the goodness of the obtained products and, possibly, improve the reliability of the system that generated them.

Starting from fig 5.1, an overview of daytime and night-time measurements is presented. SCC and UPC processed depolarization ratios products are compared during different aerosols load situations.

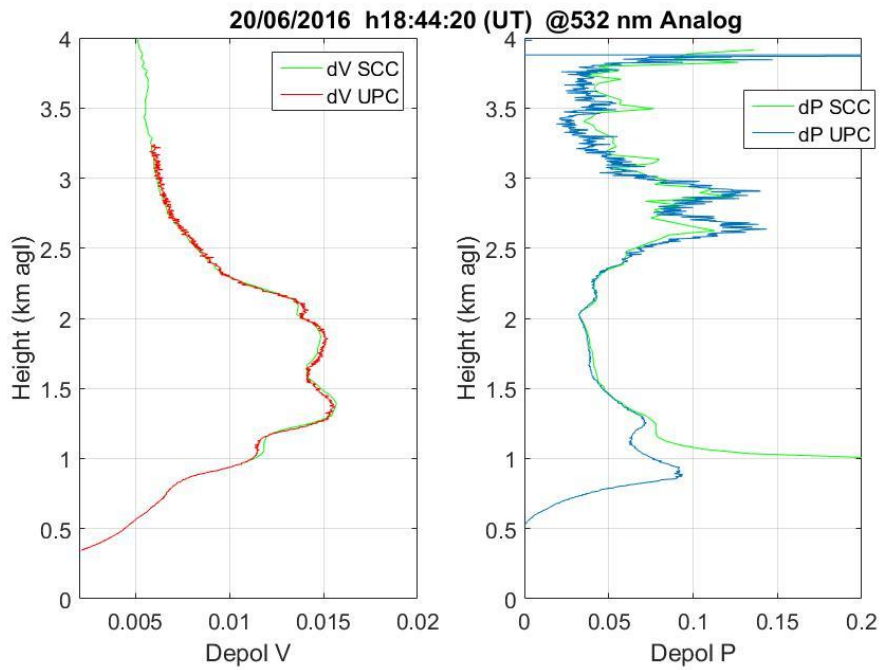


fig 5.1

Comparison between δV and δP derived with UPC and SCC algorithms from a 60 min daytime measurement on 20/06/2016 at 18:44 UT. The reference calibration is dated 01/06/2016

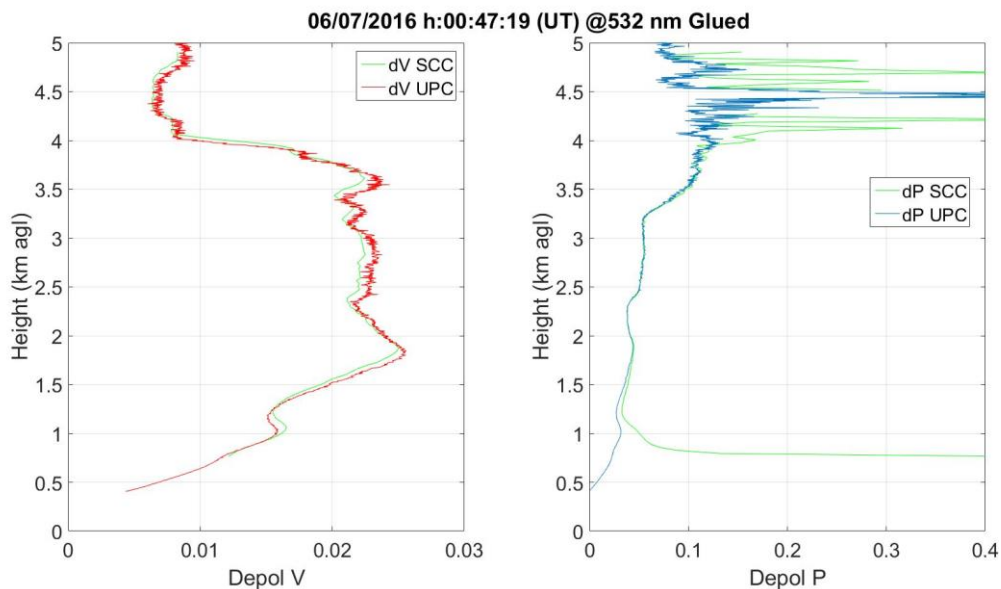


fig 5.2

Comparison between δV and δP derived with UPC and SCC algorithms from a 150 min night-time measurement on 06/07/2016 at 00:47 UT. The reference calibration is dated 05/09/2016.

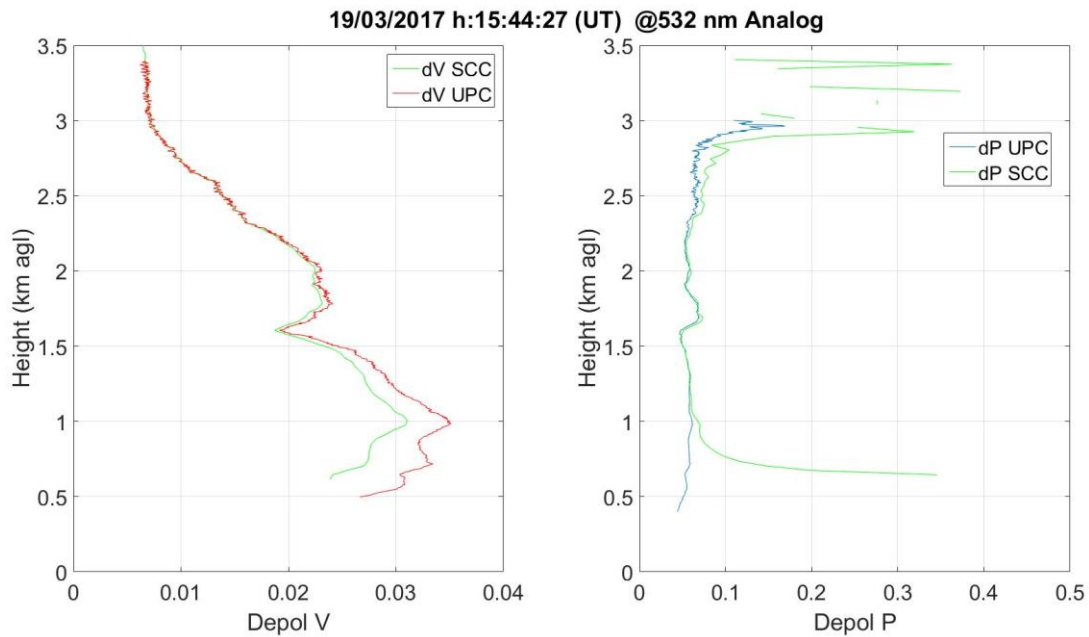


fig 5.3

Comparison between δV and δP derived with UPC and SCC algorithms from a 60 min daytime measurement on 19/03/2017 at 15:44 UT. The reference calibration is dated 15/03/2017.

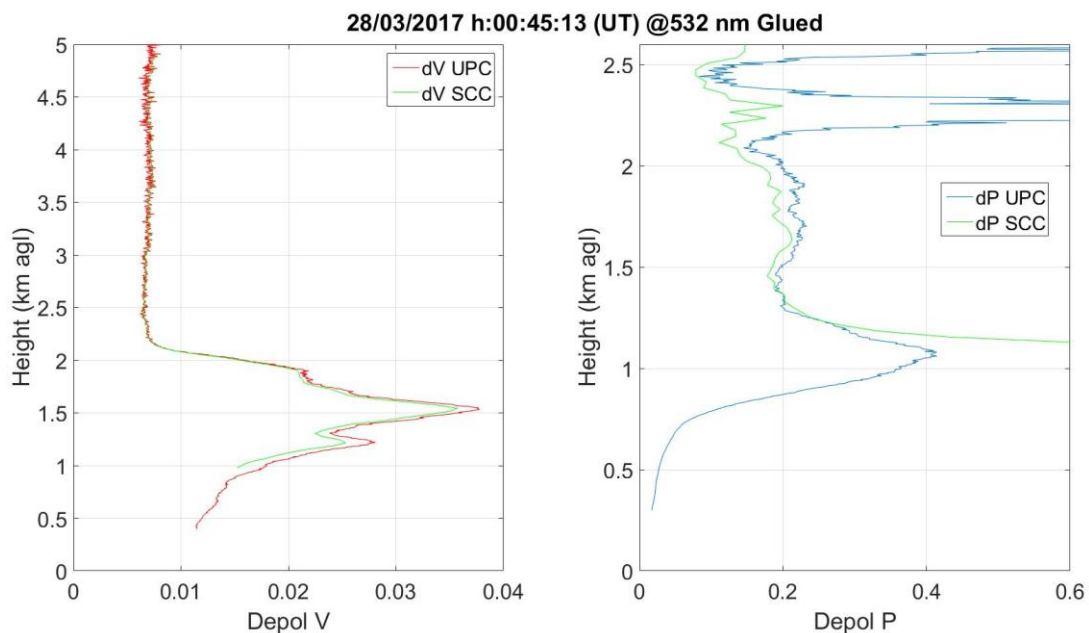


fig 5.4

Comparison between δV and δP derived with UPC and SCC algorithms from a 150 min night-time measurement on 28/03/2017 at 00:45 UT. The reference calibration is dated 15/03/2017. Concerning the δP curve, the plot has been edited to show only the region below the molecular zone. ($H < 2.5$ km)

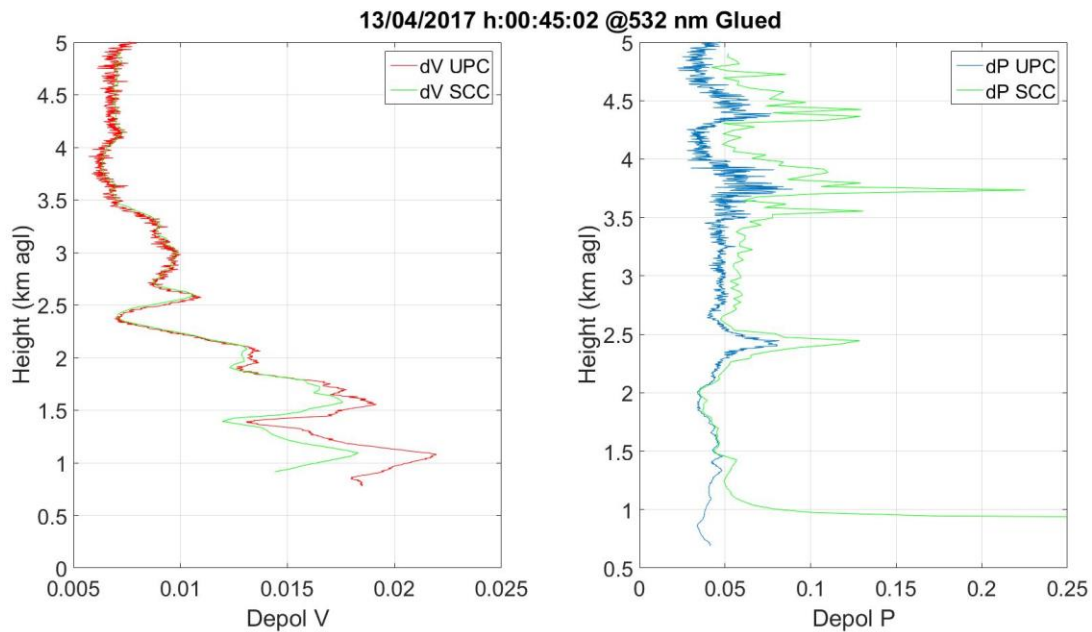


fig 5.5

Comparison between δV and δP derived with UPC and SCC algorithms from a 150 min night-time measurement on 13/04/2017 at 00:45 UT. The reference calibration is dated 15/03/2017.

Thanks to this overview it is possible to notice that there is an overall agreement between the depolarization ratios derived with SCC and UPC algorithms. Such an agreement happens to be more evident in the case of volume depolarization ratios rather than in the case of particle depolarization ratios where, on the contrary, a slight discrepancy, especially at high altitude, is present. In this region, called *molecular zone* and identified by low and constant values of δV (see fig5.3, 5.4 and 5.5), the low presence of particles induces a great alteration of δP values because such a computation is, intuitively, impossible.

Another important remark should be made regarding the growth of δP values at low altitudes. In this case, the most likely explanation to this odd phenomenon is the missing overlap correction factor in the SCC assessment of the backscatter coefficient. Such an information is provided to the SCC by means of an ancillary file which, probably due to a bug in the system, is not properly evaluated.

5.2: Comparison with MPL

The comparison with another co-located Lidar station, the MPL (Micro-Pulse-Lidar), can be useful to underline possible incongruences between the two systems due to their different working principles [21]. In fact, being in the same location, they should be in good accordance but differently with respect to the case of SCC comparison, where basically one is dealing with the same system measurements processed by two similar algorithms, MPL is a different system and sometimes few differences can be spotted. In the following examples, pictures with the computed volume depolarization ratio from the two systems are shown.

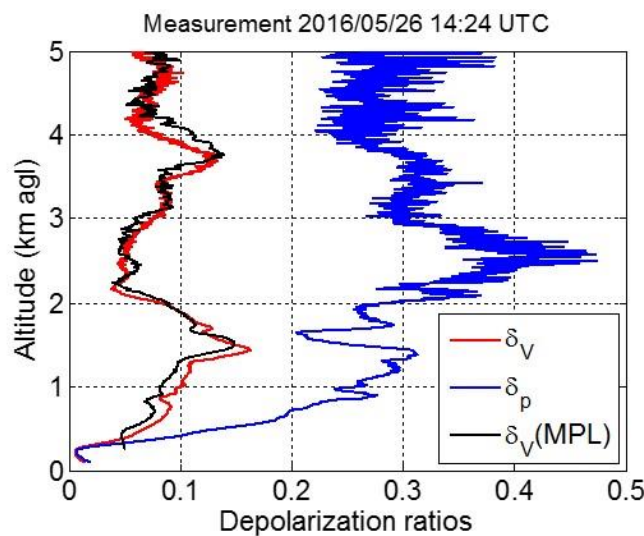


fig 5.6

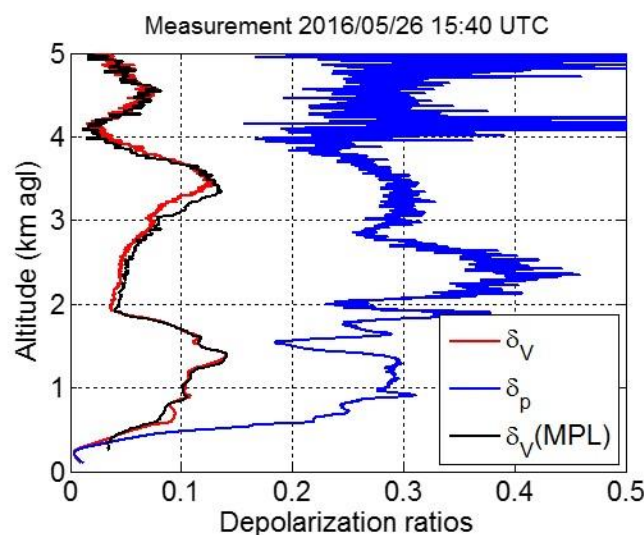


fig 5.7

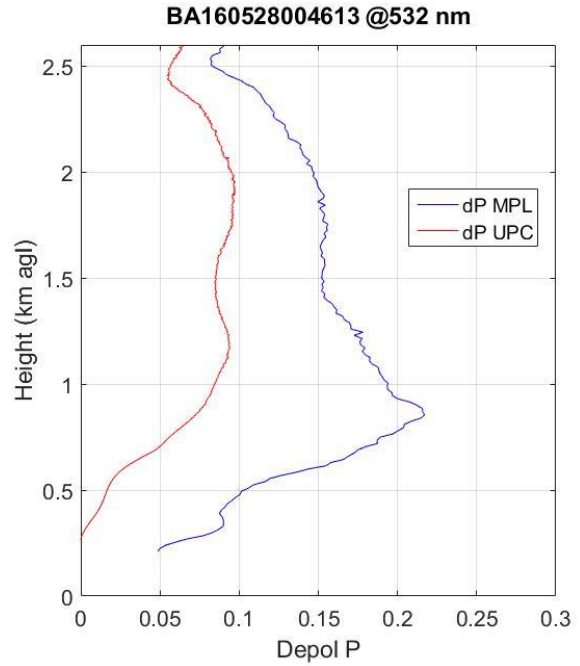
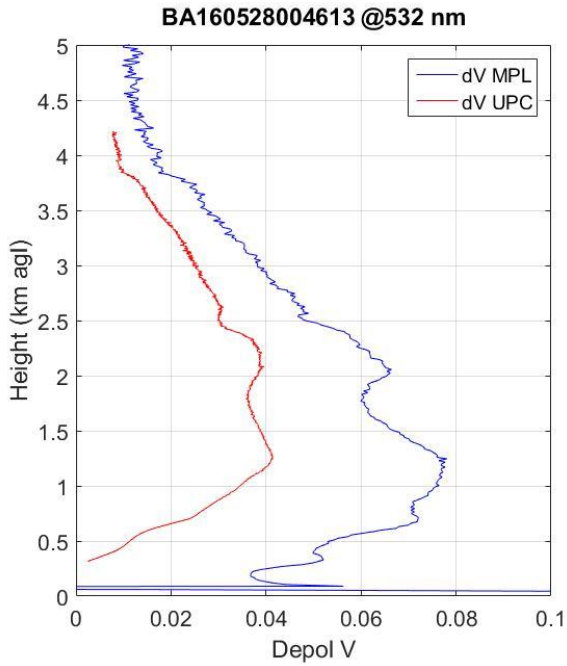


fig 5.8

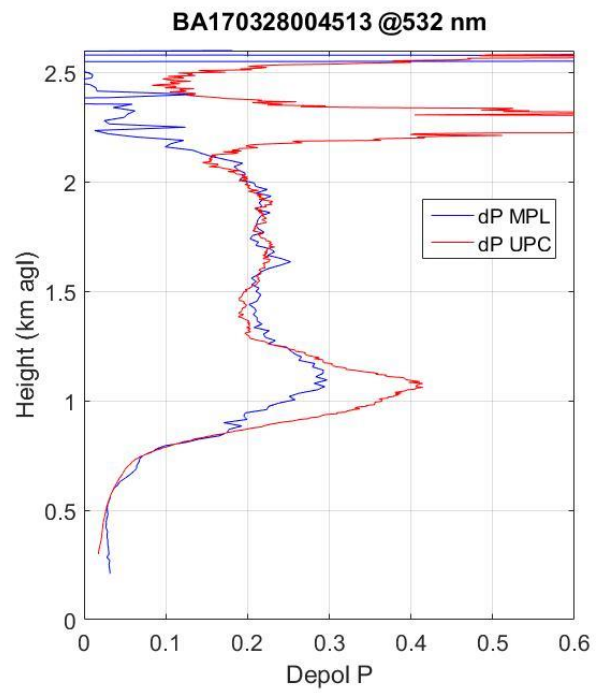
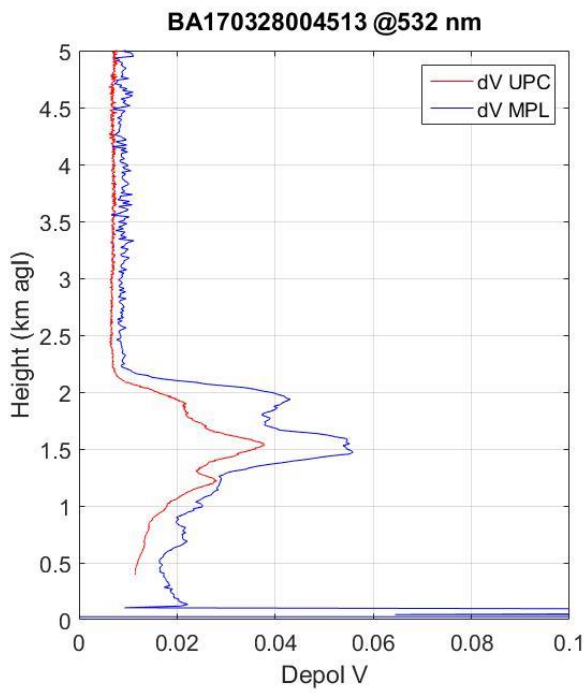


fig 5.8

Contrary to the first comparison set, in this case a huge difference between daytime and night-time can be noticed. In fact, while for daytime measurements the volume depolarization ratio seems to be in good agreement between the two different systems, for night-time measurements such an agreement is completely lost and the vertical profiles show a huge discrepancy between the values of MPL retrieval (usually high) and the ones associated to UPC profiles (usually low).

Such an odd behaviour is more investigated in fig 5.9 where three consecutive measurements taken during the LRMC (Lidar&Radiometer Measurement Campaign) campaign between 15 and 31 May 2017 are shown. During night-time, the MPL volume depolarization ratio is sometimes 1.5 time higher than the value retrieved from the UPC Lidar.

In particular, it is noticeable how in the first and the last daytime cases a good agreement is present while the spread between MPL and UPC volume depolarization ratios dramatically increases during the night.

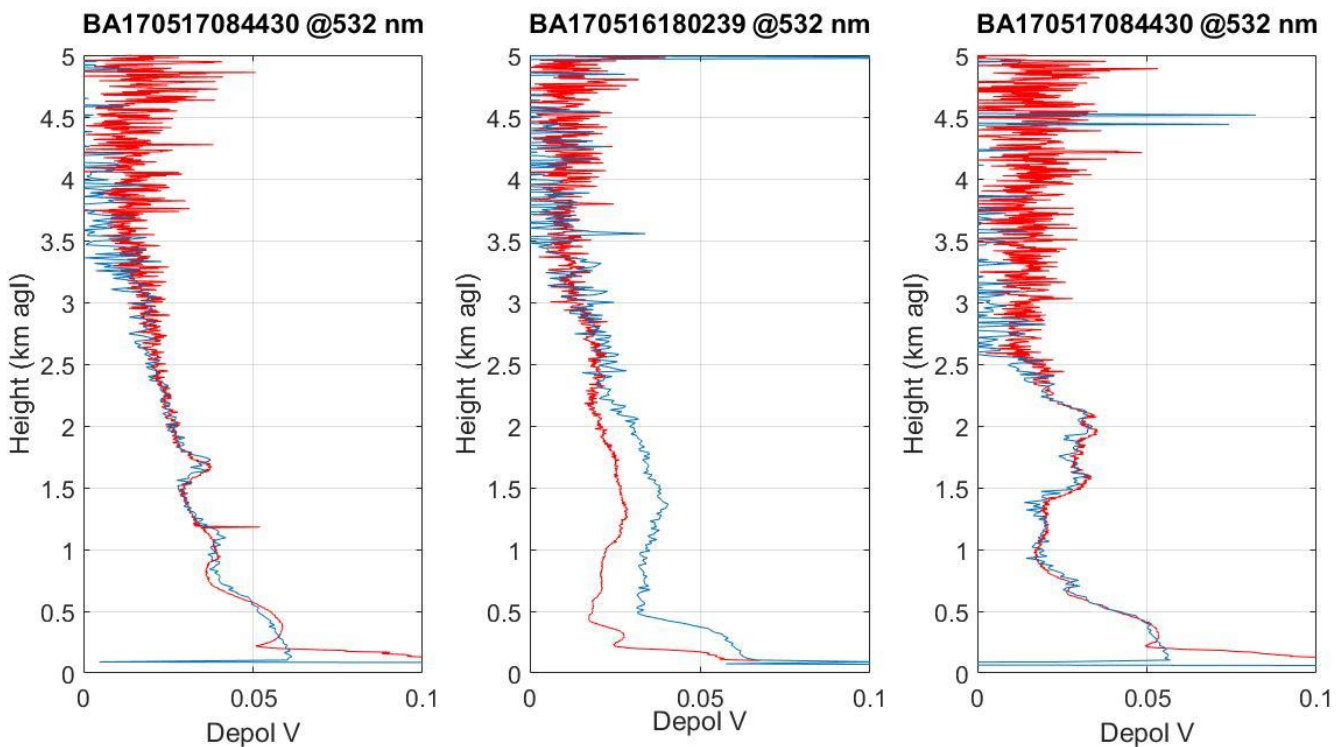


fig 5.9

Figure 5.9 shows three successive measurements performed in two days (16-17/05/2017) within ILRC campaign. It is possible to notice how during the central measurement the accordance between the two systems fails while it is recovered in the early morning measurement of the following day.

To justify such differences in night-time measurements, two explanations can be given. On the one hand, the background subtraction of the total signal may cause an underestimation of the total power. Indeed, besides the usual subtraction of background noise radiation, in case of high SNR profiles, it is possible that the far range signal still contains a bit of molecular signal, which, once subtracted, may cause an underestimation of the real useful signal. On the other hand, there is the possibility to have a malfunctioning of the MPL. In fact, the atmosphere might have changed, despite the MPL retrieved δV value holds steady during the three measurements.

5.3: Analysis of different aerosol load situations

It is now possible to analyze the result of the measurements performed in different atmospheric conditions thanks to the information given by the obtained values of δV and δP . As introduced in section 1 and 2, the study of depolarization turns out to be a useful instrument to describe the distribution (in space and time) of atmospheric aerosol. The vertical profiles give numerical evaluation of the quantity of depolarized light, providing a detailed description of the particles layers which can be found in the troposphere both in ordinary urban condition and in presence of common natural events (Saharan dust phenomena, fires, pollen intrusions etc...) ^[23]. The following analysis describe the presence of aerosol in the lower part of the troposphere. Its presence is noticeable as an increase of value of depolarization with respect to what a purely molecular atmosphere would give. In fig 5.1, for instance, it is possible to see how δV (with its error bar) profile changes in altitude during a night-time measurement in March 2017

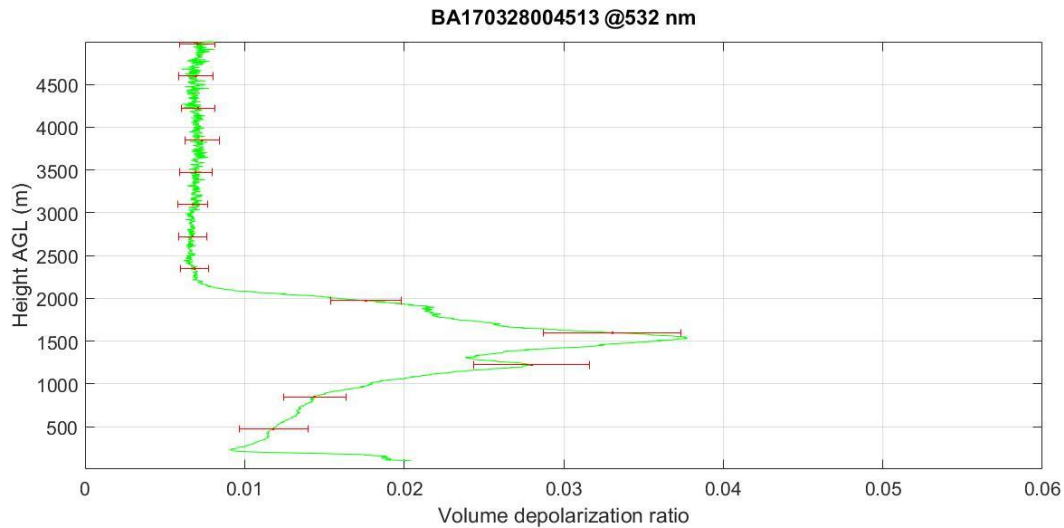


fig 5.10

Volume depolarization ratio of an aerosol layer at low altitude

In fig 5.10, the presence of aerosol can be easily identified by the growth of depolarization values. After this aerosol layer, which extends for more than 1 km, is the *molecular zone*, a layer of the troposphere where the absence of aerosol or any other depolarizing particle represents a good reference value. The presence of an aerosol layer concentrated at low altitude is more common in night-time measurements than during the day when, because of daily urban activity, aerosols are more likely to move upward.

In figure 5.11 δV and δP belonging to the previous measurement are present. While the former provides a quick way to detect the presence of depolarizing particles, the latter parameter gives a better understanding of which particles are depolarizing incident light. For this reason, of course, the range of interest now does not overcome 2 km in altitude for the evaluation of the particle depolarization ratio in molecular zone is meaningless.

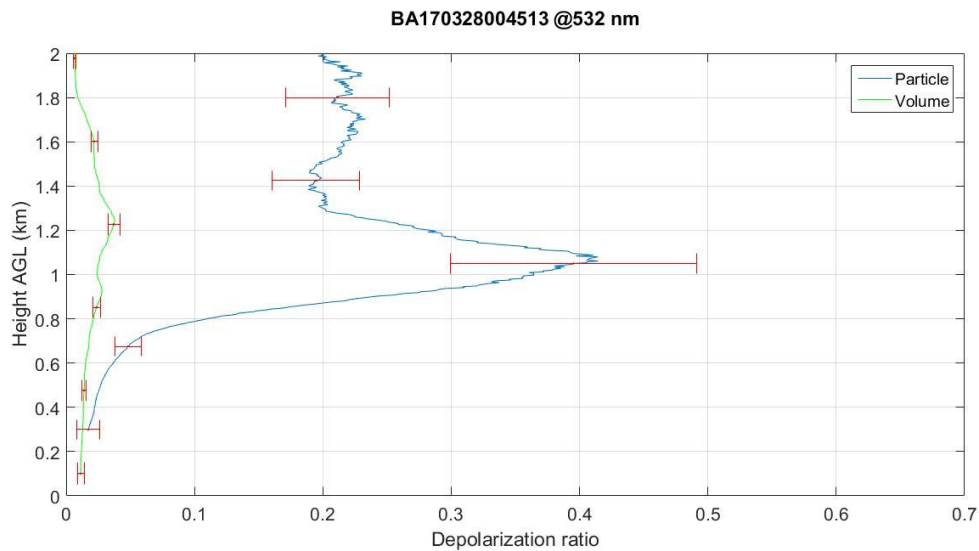


fig 5.11
Comparison of volume and particle depolarization ratio.

In fig 5.12, it is possible to notice how during a daytime measurement a larger number of aerosol layers distribute up to 4 km in altitude. Besides, the level of volume depolarization itself is much higher than in the previous case.

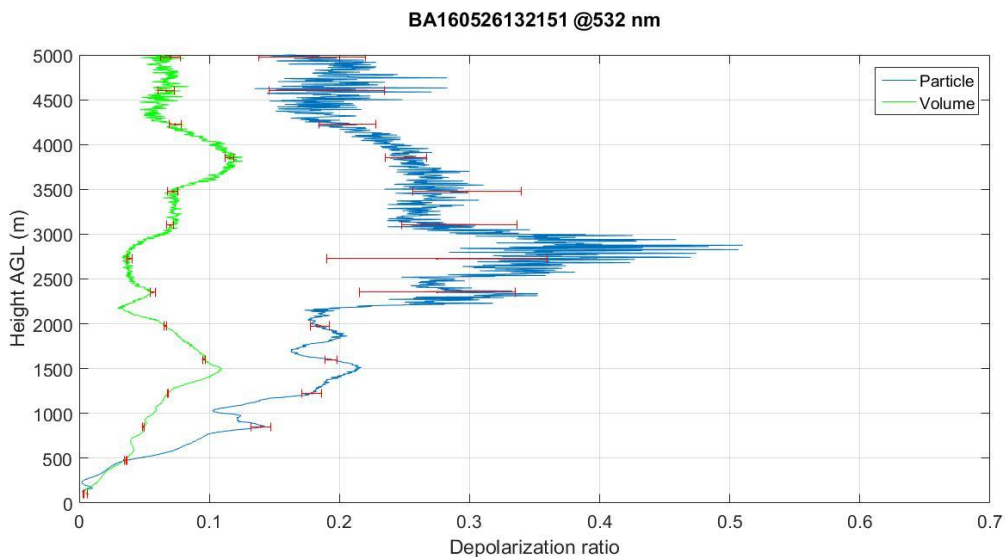


fig 5.12
Daytime comparison between Volume and Particle depolarization ratio

Although useless from the standpoint of the study of the atmosphere, an interesting case which can be seen in the following picture is the response to the presence of a low clouds. In fig 5.13 a strong peak of volume depolarization profile is present at 200 m of altitude. Such huge values are always related to a cloud. In fact, clouds cause an alteration of depolarization

values due to the multiple scattering that their molecules and droplets induce. Besides, they provoke also the complete screening of the atmosphere above them because of the very little amount of power which can get through them and come back. For this reason, a cloudy weather is not recommended for measurements unless clouds are thin and high enough.

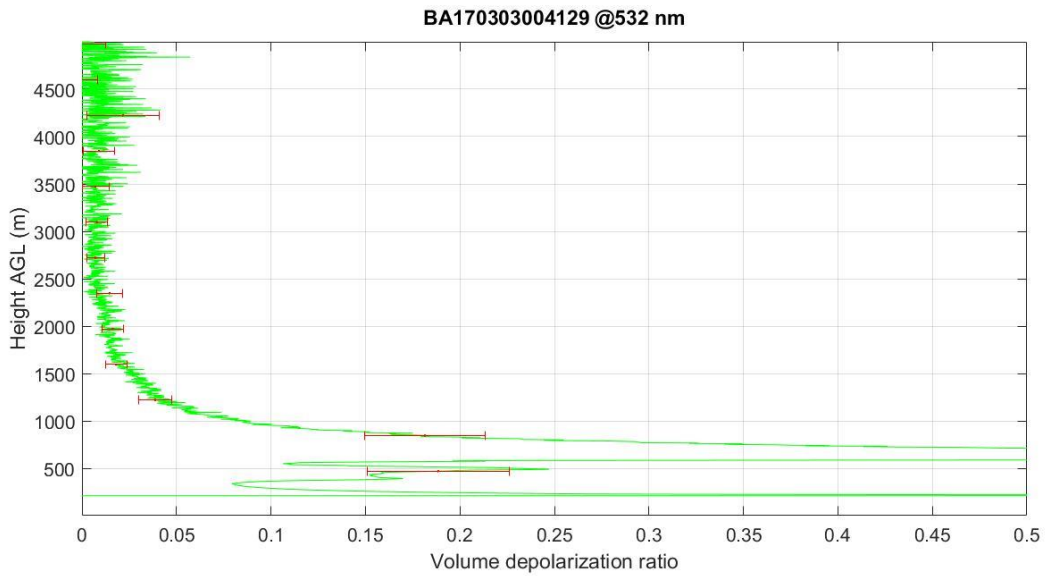


fig 5.13

Volume depolarization ratio in presence of a low cloud. The screening induced does not allow power to get through.

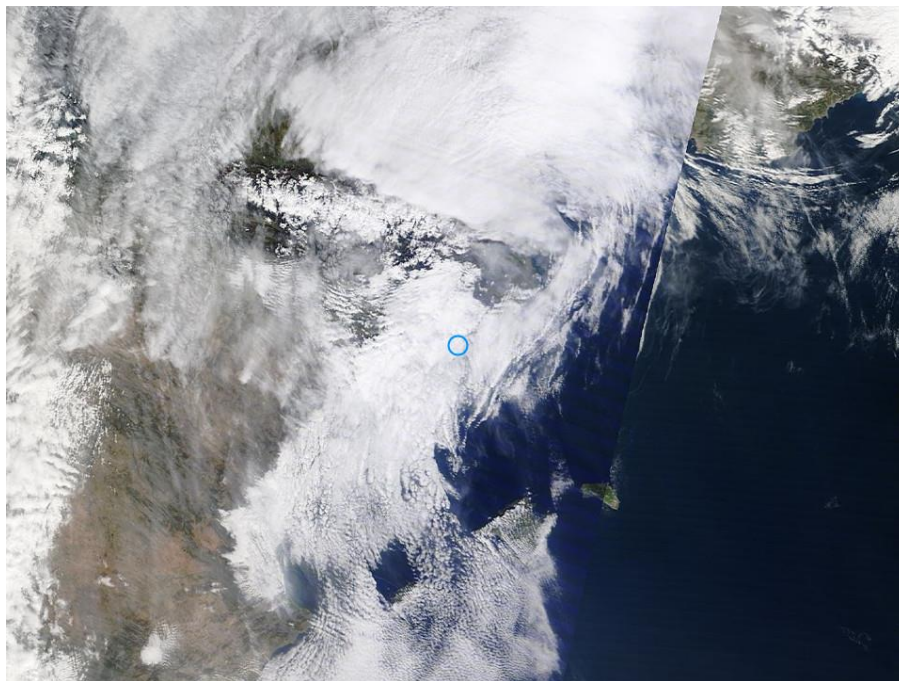


fig 5.13

MODIS map of the cloud event on 03/03/2017

Another interesting phenomenon is the result of a depolarization measurement during a Saharan dust intrusion. In fig 5.14 the result of the measurement is shown.

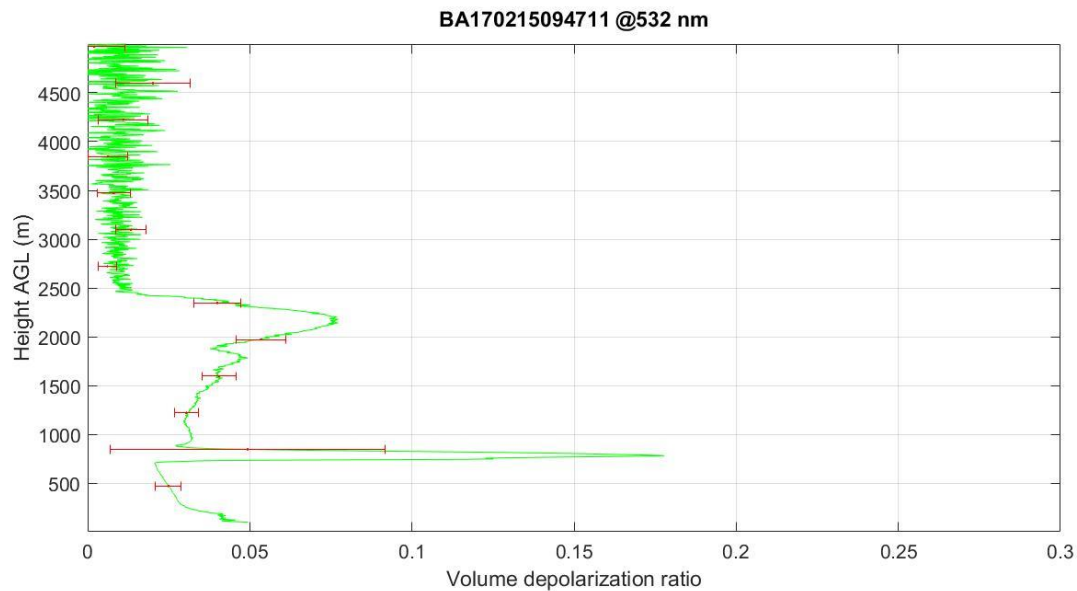


fig 5.14

Saharan dust intrusion: such a phenomenon induced a peak in the volume depolarization ratio

In this case, a volume depolarization ratio of 18% at 800 m is shown, meaning that a dense dust layer at that altitude was present. Differently from the cloud case, dust intrusions do not cause any screening whatsoever allowing the detection of aerosols in the layers above (unless they are very thick).

In fig 5.15, another outlook of the Saharan dust event already illustrated in fig 5.6 and 5.7 is shown

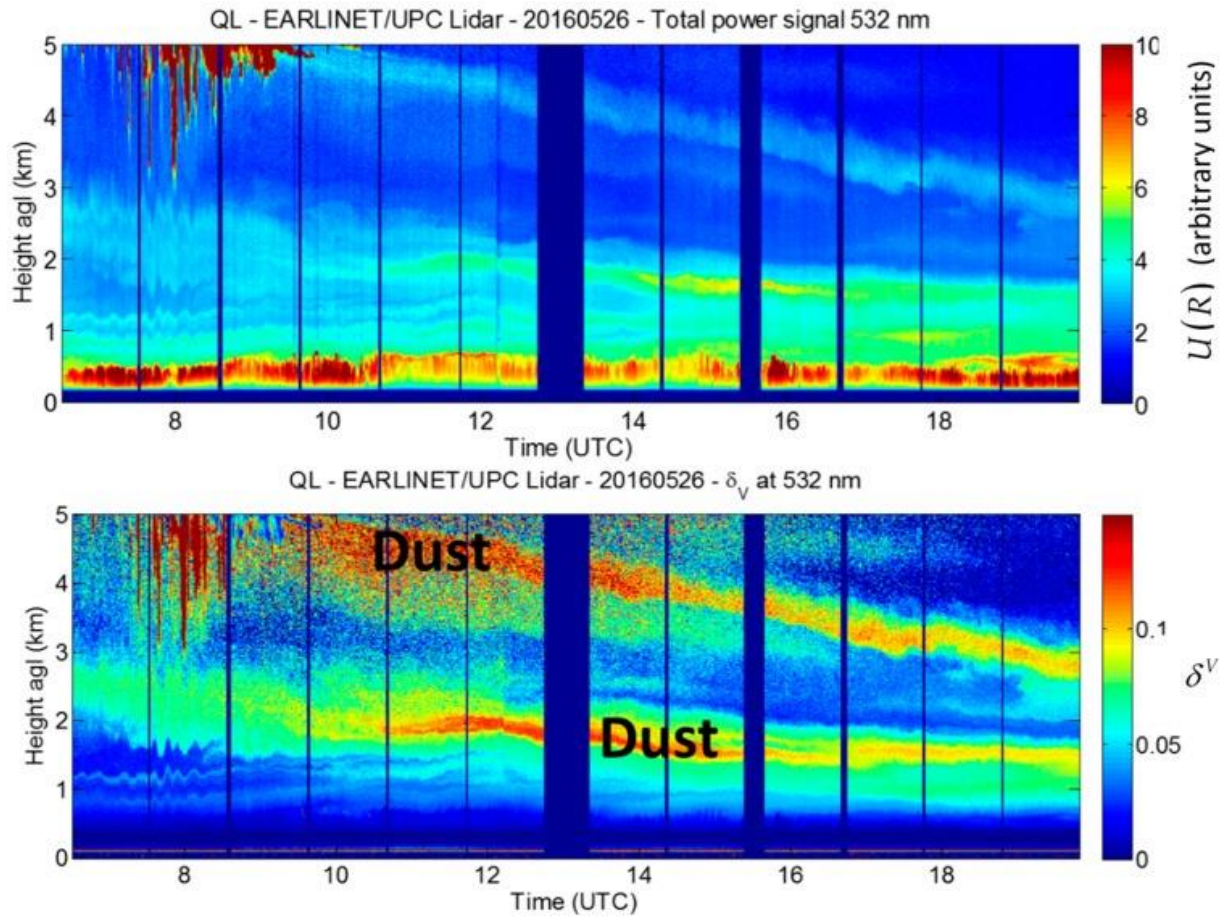


fig 5.15

Pictures 5.6 and 5.7 depict the volume and particle depolarization ratio profiles at two different hours, highlighting the presence of two layers of Saharan dust the first of which is holding steady at 1.5 km over time while the second progressively drops down. MPL volume depolarization ratio is also pictured showing great accordance between the two different systems. Picture 5.15 gives a distinct perspective showing how δ^V varies over the whole measurements hours.

Figure 5.16 shows a similar description of a weaker Saharan dust intrusion

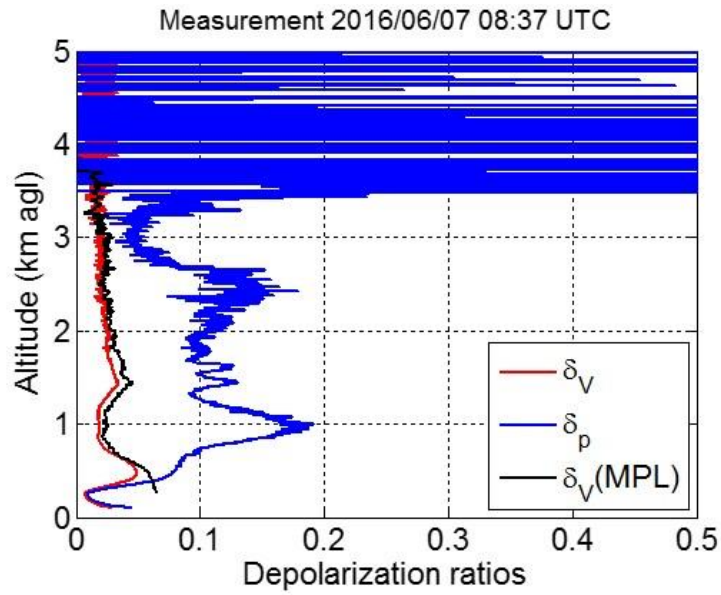


fig 5.16a

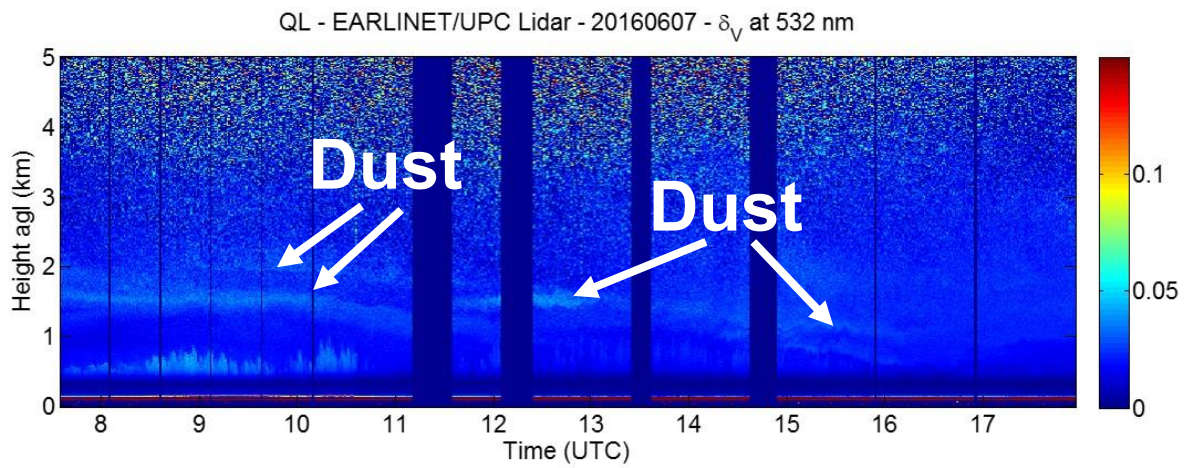


fig 5.16b

Picture showing a weaker phenomenon of Saharan dust intrusion on 07/06/2016. In this case volume depolarization ratio is below 10%

Chapter 6

Conclusions and future development

In this project, the new depolarization channel at 532 nm of the UPC lidar system has been fully characterized from an optical and mechanical point of view. The use of the optical software Zemax allowed to analyze with raytracing the real optical properties of the new channel and to compare them with the expected theoretical ones. With the actual setup the FOV was estimated to be equal to 2.85 mrad (theory: 3.3 mrad) and the spot size on the detector was estimated to be 8.8mm in diameter (inducing a signal loss of 21%). With the actual design, the rays reaching the detectors are almost paraxial, so that reducing these losses to zero would require to separate the detector from the field lens of a large distance, which, for the time being, is not physically feasible.

Concerning the calibration vectors analysis, as a first step, a statistic of the calibration vector far-range value evaluated over the last 18 months has been assessed. The results show a variation on the far-range value equal to a 10% of the maximum value within every set of calibrations defined between realignment procedures (see fig 4.4).

As a consequence, this correction has been included as a factor in the δV and δP error bar computation.

Secondly, the normalized distance between calibration vectors has been calculated in order to identify in which altitude interval is more likely to find discrepancies. This shape characterization showed a significant difference in the first 1.5 km.

Lastly, an analysis of the variation of the calibration vectors far-range values with environmental temperature has been done. As a result, a linear trend was spotted meaning that the elevated temperatures affect the system (probably dilatating metal building blocks of the channel) so to have higher values of system channel ratio.

The overall study emphasised the need to perform frequent calibrations not with the purpose of statistically reducing the error it introduces (impossible as this is a systematic error source) but to reduce the time-gap between measurement and calibration enhancing the reliability of the results.

To achieve this goal, an automatized mechanical support responsible for the rotation of the polarizer would be required.

The final analysis of the products δV and δP showed good accordance between the UPC and SCC algorithms with the only exception of low altitude δP profiles where the SCC displays high diverging values maybe due to an improper reading/correction of the overlap correction ancillary file.

The comparison of δV and δP profiles with a co-located lidar (MPL) showed huge discrepancies during night-time measurements and a reasonable agreement between daytime ones.

This issue is still under investigation by the RSLab, however it is possible to predict the outcome by studying the plausible reasons behind this problem. The two most likely causes are the different processing procedure of daytime and night-time measurements by UPC or a malfunctioning of the MPL.

In the first case the difference between the two profiles can be ascribed to an improper correction of the signal, namely, to a subtraction of part of the received molecular backscattered signal besides the usual removal of background noise radiation. This would naturally cause a decrease of the total signal.

According to the second hypothesis, on the contrary, the fallacy can be caused by MPL processing unit. In this regard, the analysis illustrated in fig 5.9 showed how the depolarization value in the low altitude range of the troposphere changed according to the two systems in two days. MPL's profile shows constancy of the results while UPC analysis does not. Although it is more likely to have similar depolarization values over a short period of time, the atmosphere could actually have changed and this would invalidate MPL results.

This represents a useful example of the importance of the synergy between different systems.

That is why EARLINET works to improve the quality of the elaborated products of SCC. An external apparatus able to assess the same analyses performed "in situ" is extremely useful for every Lidar station because, in such a way, very helpful comparisons can be made.

As a last remark, through this work it should be put in evidence the importance of the study of light depolarization for the typing of aerosols and the success of the employed channel at 532 nm leads the way to the possibility of a further extension of the system, including a depolarizing channel devoted to another working frequency of the system. Such a possibility is encouraged by the ease of the using and the rather small space occupied by a similar auxiliary channel.

As a matter of fact, as of this moment, the design of a depolarization channel also at 355 nm is being developed to broaden the capability of the present system, enhancing its potential and giving, as a result, a thorough description of our atmospheric constituents.



Appendix A

δV and δP error bars derivation

Dealing with independent physical quantities, the formula which must be applied is the general one with partial derivatives, namely

$$\Delta f = \Delta f(x_1, x_2, \dots, x_n, \Delta x_1, \Delta x_2, \dots, \Delta x_n) = \sum_{i=1}^n \left| \frac{\partial f}{\partial x_i} \right| \cdot |\Delta x_i|$$

where f is a generic function with n non-correlated variables and relative uncertainties which, under these circumstances, are assumed to be small relative random error.

- **A.1: Error bar for δ^V**

A.1.1: Sources of error considered for δ^V

Volume depolarization ratio δ^V is subject to both statistical and systemic errors. The statistical error is often related to the noise which affect the signals. This type of error is commonly reduced by means of an appropriate temporal averaging. Concerning the systematic errors, these are the most important to handle for their value cannot be statistically reduced. In the case of δ^V the main source is the calibration, and it affects the system channel ratio V^* . Performing $\pm 45^\circ$ calibrations is an appropriate choice to minimize such an error making it compensate through the double measurement. The sources of the considered errors are the following.

- The error associated to the calculation of the depolarization observable, δ^* .
- The error estimated from the stability of the calibration vector, V^* .

A.1.2: Expression of the error bars for δ^V

Starting with the computation of the error of the depolarization observable. Its error sources mainly come from photon statistic and amplification noise [4]:

$$\delta^*(90^\circ, R) = \frac{S_{\text{dep}}(90^\circ, R)}{S_{\text{tot}}(90^\circ, R)}$$

$$\text{err}(\delta^*) = \left| \frac{1}{S_{\text{tot}}} \right| \cdot |\text{err}(S_{\text{dep}})| + \left| \frac{S_{\text{dep}}}{(S_{\text{tot}})^2} \right| \cdot |\text{err}(S_{\text{tot}})|$$

Once this function is defined, it is possible to move to the expression of the Volume depolarization ratio:

$$\delta^V(R) = \frac{\delta^*(90^\circ, R)}{V^*(R) - \delta^*(90^\circ, R)}$$

$$\text{err}(\delta^V) = \left| \frac{\delta^*}{(V^* - \delta^*)^2} \right| \cdot |\text{err}(V^*)| + \left| \frac{V^*}{(V^* - \delta^*)^2} \right| \cdot |\text{err}(\delta^*)|$$

The absolute value of $\text{err}(V^*)$ is empirically deduced from the analysis of System channel ratio in the far range and is taken equal to $0.1 \cdot V_{\text{max}}^*$ (see section 4).

• A.2: Error bar for δ^P

A.2.1: Sources of error considered for δ^P

As for the case of δ^V , also in the case of particle depolarization ratio the systematic errors are usually bigger compared to the statistical errors that may come from optical and amplification noise. In this case the major contribution of systematic error is the one associated to the particle backscatter coefficient β^P . In this case, the sources of error considered are:

- The error associated to the inversion of particle backscatter coefficient, β^P , by the Klett-Fernald method.
- The error associated to the volume depolarization ratio, δ^V .

A.2.2: Expression of the error bars for δ^p

We start with δ^p definition formula:

$$\delta^p(R) = \frac{[1 + \delta^m]\delta^v(R) \cdot \rho - [1 + \delta^v(R)]\delta^m}{[1 + \delta^m] \cdot \rho - [1 + \delta^v(R)]}$$

where

$$\delta^m = \frac{\beta_{\perp}^m}{\beta_{\parallel}^m} \qquad \rho = \frac{\beta}{\beta^m} = \frac{\beta^m + \beta^p}{\beta^m}$$

In particular, at first, the expression of the systematic uncertainty associated to ρ must be found:

$$\text{err}(\rho) = \left| \frac{1}{\beta^m} \right| \cdot |\text{err}(\beta^p)|$$

Given the value of the particle backscatter coefficient error, one can evaluate the error affecting the particle depolarization ratio, taking also into account the contributions of δ^v uncertainty, working it properly in the formula according to error propagation rules:

$$\begin{aligned} \text{err}(\delta^p) = & \left| \frac{[(1 + \delta^m)\rho - \delta^m] \cdot [(1 + \delta^m) \cdot \rho - (1 + \delta^v)] + [(1 + \delta^m)\delta^v\rho - (1 + \delta^v)\delta^m]}{[(1 + \delta^m) \cdot \rho - (1 + \delta^v)]^2} \right| \cdot |\text{err}(\delta^v)| + \\ & + \left| \frac{[(1 + \delta^m)\delta^v] \cdot [(1 + \delta^m) \cdot \rho - (1 + \delta^v)] - (1 + \delta^m) \cdot [(1 + \delta^m)\delta^v\rho - (1 + \delta^v)\delta^m]}{[(1 + \delta^m) \cdot \rho - (1 + \delta^v)]^2} \right| \cdot |\text{err}(\rho)| \end{aligned}$$

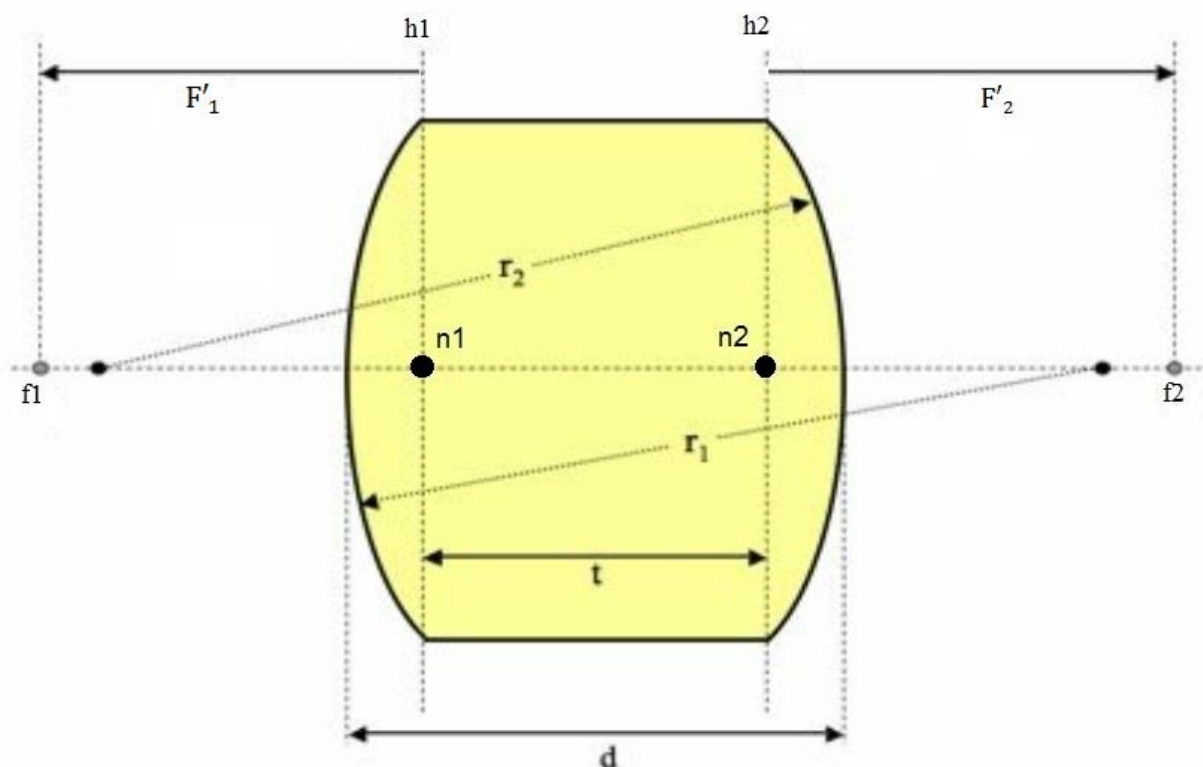
Once rearranged, the error associated to δ^p writes:

$$\text{err}(\delta^p) = \left| \frac{(1 + \delta^m)^2 \rho (\rho - 1)}{[(1 + \delta^m) \cdot \rho - (1 + \delta^v)]^2} \right| \cdot |\text{err}(\delta^v)| + \left| \frac{(1 + \delta^m) \cdot (1 + \delta^v) \cdot (\delta^m - \delta^v)}{[(1 + \delta^m) \cdot \rho - (1 + \delta^v)]^2} \right| \cdot |\text{err}(\rho)|$$

Appendix B

Matlab sequence steps for transmission matrix evaluation in a thick lens analysis.

- **Definition of cardinal quantities**



There are 6 cardinal quantities to be defined in a thick lens system^[15]:

2 system focal points: f_1 and f_2
 2 system principal planes: h_1 and h_2
 2 system nodal points: n_1 and n_2

where

1-subscript is related to left surface

2-subscript is related to right surface

The employed scheme follows the convention according to which focal distances are considered with respect to the principal planes, distances towards the right are considered positive and distances towards the left are considered negative

In the most general case we have 3 media to consider, the inner one, and the two external ones. So, in such a case, the formula used to evaluate the focal length is:

$$\frac{1}{f_1} = \frac{n_G - n'}{nR_2} - \frac{n_G - n}{nR_1} - \frac{(n_G - n)(n_G - n')}{nn_G} \cdot \frac{t}{R_1R_2}$$

Where

n_G is the lens material refractive index

n is the left material refractive index

n' is the right material refractive index

t is the lens thickness

R_1 is the left radius of curvature

R_2 is the right radius of curvature

From the previous formula one derives all the others cardinal points

$$f_2 = -\frac{n'}{n} f_1$$

and to locate the principal planes one has simply to use the following two formulas

$$r = \frac{n_G - n'}{n_G R_2} t f_1 \qquad s = -\frac{n_G - n}{n_G R_1} t f_2$$

These last two are measure of the distance between the surface vertex and the plane

• Matrix method

There are two exploited matrices: translation matrix and refraction matrix

The former describes the simple propagation of a ray in a homogeneous medium. The only parameter which matters is its length.

$$T = \begin{bmatrix} 1 & L \\ 0 & 1 \end{bmatrix}$$

Where L is the medium length.

The latter matrix describes the refraction of a ray when crossing a spherical surface having a radius of curvature equal to r, which stands between two materials having refractive index n and n'

$$R = \begin{bmatrix} 1 & 0 \\ \frac{1}{r} \left(\frac{n}{n'} - 1 \right) & \frac{n}{n'} \end{bmatrix}$$

Once the two matrices are defined, the whole structure might be described as a succession of these matrices describing the path a ray covers, made of refraction at surfaces and translations in media.

So, according to the number of surfaces which are present in the structure, one is able to define the complete matrix.

In this regard, one important remark must be made. Since matrices multiplication is not commutative and their order is relevant. In particular, in this case, it is necessary to start from the latest surface on the right up to the first surface on the left.

Having the complete matrix, it is possible to retrieve the focal length and all the other key parameters.

$$M = \begin{bmatrix} A & B \\ C & D \end{bmatrix}$$

For instance, the two global focal lengths (relative to reference planes) are defined as

$$F_1 = \frac{D}{C} \qquad F_2 = -\frac{A}{C}$$

whilst the focal lengths relative to the principal planes are defined as

$$F'_1 = \frac{n/n'}{C}$$

$$F'_2 = -\frac{1}{C}$$

Concerning the case under analysis in section 3, the complete matrix retrieved in the two approaches are the following.

The multiplication to get the total matrix involves 11 matrices, accounting for the 6 refracting surfaces (2 for each lens) and 5 media (3 glasses and 2 air):

$$M_{\text{tot}} = \begin{bmatrix} 1 & 0 \\ \frac{1}{R_{3,2}} \left(\frac{n_g}{n_a} - 1 \right) & \frac{n_g}{n_a} \end{bmatrix} \cdot \begin{bmatrix} 1 & T_3 \\ 0 & 1 \end{bmatrix} \cdot \begin{bmatrix} 1 & 0 \\ \frac{1}{R_{3,1}} \left(\frac{n_a}{n_g} - 1 \right) & \frac{n_a}{n_g} \end{bmatrix} \cdot \dots \cdot \begin{bmatrix} 1 & 0 \\ \frac{1}{R_{1,2}} \left(\frac{n_g}{n_a} - 1 \right) & \frac{n_g}{n_a} \end{bmatrix} \cdot \begin{bmatrix} 1 & T_1 \\ 0 & 1 \end{bmatrix} \cdot \begin{bmatrix} 1 & 0 \\ \frac{1}{R_{1,1}} \left(\frac{n_a}{n_g} - 1 \right) & \frac{n_a}{n_g} \end{bmatrix}$$

Where

n_a is the air refractive index;

n_g is the glass refractive index;

$R_{x,y}$ is the radius of curvature of surface y of lens x ;

T_x is the central thickness of lens x ;

As far as *trial-and-error* approach is concerned:

$$M_{\text{tot } 1} = \begin{bmatrix} 0.3780 & 126.8268 \\ -0.0029 & 1.6867 \end{bmatrix}$$

As a result, one gets:

$$F_1 = -581.62$$

$$F_2 = 130.34$$

$$F'_2 = -F'_1 = 344.82$$

While for the Zemax-approximated case:

$$M_{\text{tot } 2} = \begin{bmatrix} 0.4547 & 126.8664 \\ -0.0033 & 1.2860 \end{bmatrix}$$

As a result, one gets:

$$F_1 = -389.69$$

$$F_2 = 137.79$$

$$F'_2 = -F'_1 = 303.03$$



BIBLIOGRAPHY

- [1] IPCC (2007). Climatechange2007: The physical science basis. *Contribution of working group I to the fourth assessment report of the intergovernmental panel on climate change. Technical report, Intergovernmental Panel on Climate Change, Cambridge University Press, Cambridge, United Kingdom and New York, NY, USA.*
- [2] E. Calvo (2013) “Design of a depolarization channel at 532 nm for the UPC EARLINET lidar”
Career final project Dissertation. Departamento de Teoría de la Señal y Comunicaciones. Escuela Técnica Superior de Ingeniería de Telecomunicación de Barcelona. Universitat Politècnica de Catalunya, Barcelona, Spain.
- [3] M. Tesche [et al] (2009) “Vertical profiling of Saharan dust with Raman lidars and airborne HSRL in southern Morocco during SAMUM,”
Tellus, Ser. B Chem. Phys. Meteorol., vol. 61, 1, pp. 144–164.
- [4] V. Freudenthaler [et al] (2009) “Depolarization ratio profiling at several wavelengths in pure Saharan dust during SAMUM 2006”
Tellus, 61B, pp. 165-179.
- [5] K. Sassen (2005), “Polarization in Lidar,”
in Lidar, C. Weitkamp, Ed. New York: Springer-Verlag, pp. 19–42.
- [6] Claus Weitkamp (2005) “Lidar: Range-Resolved Optical Remote Sensing of the Atmosphere”
New York Springer, pp. 1-40.
- [7] A. Comerón (2005) “Lidar Techniques for remote sensing of the atmosphere”
13th International School of Quantum electronics, SPIE vol. 5830, pp. 296-306
- [8] F. Fernald (1984) “Analysis of atmospheric lidar observations, some comments”.
Applied Optics, 23, pp. 652–653
- [9] D. Kumar (2012) “Concept Design, Analysis and Integration of the New U.P.C Multispectral Lidar System”
Ph.D thesis Dissertation. Departamento de Teoría de la Señal y Comunicaciones. Escuela Técnica Superior de Ingeniería de Telecomunicación de Barcelona. Universitat Politècnica de Catalunya, Barcelona, Spain.

[10] A. Rodríguez-Gómez (2016) “First particle depolarization ratio measurements at the Barcelona (Spain) EARLINET/ACTRIS station: developments, implementation and first results”

Presentation at RICTA 2016, Aveiro P.

[11] B. A. Angstrom and T. Eppley (1964) “The parameters of atmospheric turbidity,” *Tellus*, vol 16, 1, pp. 64-75.

[12] U. Wandinger et al (2008) “CALIPSO and beyond: long-term ground-based support of space-borne aerosol and cloud lidar missions”.

Proc. of the 24th International Laser Radar Conference, Boulder, CO (USA), 2008, pp. 715-718 (Vol II).

[13] Zenit Camera, Datasheet, “TAIR-3S Telephoto lens”

<http://www.zenitcamera.com/archive/lenses/tair-3.html>

[14] ZEBASE (2003) “Optical Design Database: User’s Guide”

Zemax Development Corporation, version 5.0

[15] E. Hact (2007) “Optics”

Fourth edition, Addison Wesley, 2007

[16] ZEMAX (2006) “Optical Design Program: User’s Guide”

Zemax Development Corporation.

[17] V. Freudenthaler (2016) “About the effects of polarising optics on lidar signals and the $\Delta 90$ calibration”

Atmospheric Measurement Techniques, 9, pp. 4181-4255.

[18] I. Mattis [et al] (2009) “Systematic error of lidar profiles caused by a polarization-dependent receiver transmission: quantification and error correction scheme”

Applied Optics, pp. 2742-2751

[19] M. Sicard [et al] (2009) “Aerosol Lidar Intercomparison in the Framework of SPALINET—The Spanish Lidar Network: Methodology and Results”

IEEE Transactions on geoscience and remote sensing, vol. 47, 10, pp. 3547-3559

[20] F. Rocadenbosch [et al] (2008) “THE EUROPEAN AEROSOL RESEARCH LIDAR NETWORK (EARLINET): AN OVERVIEW”

Conference: IEEE International Geoscience & Remote Sensing Symposium, IGARSS 2008, July 8-11, 2008, Boston, Massachusetts, USA, Proceedings.

- [21] MICRO PULSE LIDAR SYSTEM: MPL-4B-IDS Series (2012) “Instruction Manual”
SigmaSpace, pp.16-19.
- [22] G. D’Amico [et al] (2015), “EARLINET Single Calculus Chain – overview on methodology and strategy”
Atmospheric Measurement Techniques, 8, pp. 4891–4916.
- [23] M. Sicard [et al] (2011) “Seasonal variability of aerosol optical properties observed by means of a Raman lidar at an EARLINET site over Northeastern Spain”
Atmospheric Chemistry and Physics, 11, 175-190.
- [24] V. Freundenthaler “EFFECTS OF SPATIALLY INHOMOGENEOUS PHOTOMULTIPLIER SENSITIVITY ON LIDAR SIGNALS AND REMEDIES”
Meteorologisches Institut der Universität München, Munich, Germany.
- [25] A. Behrendt, T. Nakamura (2002) “Calculation of the calibration constant of polarization lidar and its dependency on atmospheric temperature”
Optical Society of America, pp. 805-817.

Textbooks

E. D. Hinkley (1976), “Topics in Applied Physics: Laser Monitoring of the Atmosphere”,
Volume 14, Springer-Verlag.

V. A. Banakh, V. L. Mironov (1987) “LIDAR IN A TURBULENT ATMOSPHERE”,
Artech House.

E. Hact (2007) “Optics”
Fourth edition, Addison Wesley.

